

A general isogeometric finite element formulation for rotation-free shells with embedded fibers and in-plane bending

Thang X. Duong^{a,b}, Mikhail Itskov^{b,1}, and Roger A. Sauer^{a,c,d,2}

^a*Aachen Institute for Advanced Study in Computational Engineering Science (AICES), RWTH Aachen University, Templergraben 55, 52056 Aachen, Germany*

^b*Department of Continuum Mechanics, RWTH Aachen University, Templergraben 55, 52056 Aachen, Germany*

^c*Faculty of Civil and Environmental Engineering, Gdańsk University of Technology, ul. Narutowicza 11/12, 80-233 Gdańsk, Poland*

^d*Department of Mechanical Engineering, Indian Institute of Technology Kanpur, UP 208016, India*

Abstract: This paper presents a general, nonlinear finite element formulation for rotation-free shells with embedded fibers that captures anisotropy in stretching, shearing, twisting and bending – both in-plane and out-of-plane. These capabilities allow for the simulation of large sheets of heterogeneous and fibrous materials either with or without matrix, such as textiles, composites, and pantographic structures. The work is a computational extension of our earlier theoretical work (Duong et al., 2021) that extends existing Kirchhoff-Love shell theory to incorporate the in-plane bending resistance of initially straight or curved fibers. The formulation requires only displacement degrees-of-freedom to capture all mentioned modes of deformation. To this end, isogeometric shape functions are used in order to satisfy the required C^1 -continuity for bending across element boundaries. The proposed formulation can admit a wide range of material models, such as surface hyperelasticity that does not require any explicit thickness integration. To deal with possible material instability due to fiber compression, a stabilization scheme is added. Several benchmark examples are used to demonstrate the robustness and accuracy of the proposed computational formulation.

Keywords: nonlinear Kirchhoff-Love shells; in-plane bending; isogeometric analysis; fibrous composites; strain gradient theory; material instability.

1 Introduction

The computational simulation of fiber reinforced composites has become an essential tool in designing products, for example in the automotive, aerospace, biomedical and sports industry. Besides, computational simulations play an important role in analyzing the production process of such composite materials itself. For example, for woven and non-crimp fabric composites, this process can include the production of textile fabrics, the stacking of fabric layers, the draping and fixation of the stack to the desired shape in a mould, and the injection of matrix materials into the mould for bonding fibers in the final product. Likewise, simulations help in designing pantographic structures and designing reinforcement layouts for reinforced concrete structures.

In the above mentioned applications, finite shell elements based on the classical Cauchy continuum are predominantly used to model textile fabrics (e.g. see Yu et al. (2005); Boisse et al. (2008, 1997); Khiêm et al. (2018)). This choice usually provides a good prediction of the overall behavior of fabrics, especially for fibers strongly bonded to the matrix. However, it fails to

¹corresponding author, email: itskov@km.rwth-aachen.de

²corresponding author, email: sauer@aices.rwth-aachen.de

reproduce localized deformations due to the in-plane bending resistance of embedded fibers. The influence of the in-plane bending stiffness becomes significant when there is a large change in the in-plane curvature. This happens for example in shear bands occurring when dry fabrics are deformed (Boisse et al., 2017). Numerical simulations using Cauchy-based shell formulations will fail to converge to a finite width of the shear bands. Essentially, the classical Cauchy continuum, and numerical methods based on it, are inconsistent with the observed behavior.

The in-plane bending stiffness can affect not only the localized deformation, but also the global deformation. This is shown in Madeo et al. Madeo et al. (2016) and Barbagallo et al. Barbagallo et al. (2017) for the bias extension test of so-called unbalanced woven fabrics, where the in-plane bending stiffness varies between fiber families. As observed in the experiment (Madeo et al., 2016; Barbagallo et al., 2017), the global deformation is asymmetric. Numerical simulations with Cauchy-based shell formulations will also fail to produce such shapes.

The inability to respond to in-plane bending deformations is due to the underlying fundamental assumption of the Cauchy continuum that the corresponding bending moment vanishes at a material point. A more general continuum model is thus required and can be provided by strain gradient theories, see e.g. Mindlin and Tiersten (1962); Koiter (1963); Toupin (1964); Mindlin (1965); Germain (1973). Many theoretical works have adapted strain gradient theories to incorporate fiber bending, e.g. in fiber-reinforced solids (Spencer and Soldatos, 2007; Soldatos, 2010; Steigmann, 2012), fiber-reinforced composites (Steigmann and Dell’Isola, 2015; Asmanoglo and Menzel, 2017), and shells (Steigmann, 2018; Balabanov et al., 2019).

In the literature, there exist also computational models for gradient theory. Ferretti et al. Ferretti et al. (2014) present a computational formulation for a so-called constrained micromorphic theory including a second-gradient³ model, like the one of Germain Germain (1973), as a special case. In order to reproduce the bias extension test for unbalanced fabrics, Madeo et al. Madeo et al. (2016) further extended the constrained micromorphic continuum model and its corresponding numerical formulation such that it can capture the change in the relative fiber angles, the variation of the bending stiffness between fiber families, and also the relative slipping of the tows. A finite element formulation for the gradient model of Spencer and Soldatos Spencer and Soldatos (2007) was presented by Asmanoglo and Menzel Asmanoglo and Menzel (2017). Here, the C^1 -continuity requirement for the second-gradient terms is relaxed by additional field variables coupled to the deformation gradient.

The computational formulations mentioned so far have focused only on plane strain problems. A general second-gradient shell formulation that explicitly accounts for in-plane fiber bending, as considered here, is still missing. It is worth noting that there are also discrete formulations capable of capturing in-plane bending, either using interacting particles (Battista et al., 2017), or grids of Euler–Bernoulli beams interconnected by pivots at the intersection points (D’Agostino et al., 2015), or interconnected by rotational and translational elastic springs (Madeo et al., 2016).

An important development of recent years are high order approximation methods that provide a more accurate and smoother description of computational domains. In particular, the advent of so-called *isogeometric analysis* (IGA) (Hughes et al., 2005) offers significant advantages over the classical finite element method. Its ability to describe a surface with high accuracy and smoothness facilitates the recent advancement of so-called *rotation-free* shell formulations. In such formulations, the unknowns per node contain only three displacement degrees-of-freedom, while rotations are obtained from the surface displacement. This is feasible when the discretized geometry is smooth and accurate. Therefore, the combination of IGA with rotation-free shells

³i.e. the second displacement gradient

can increase both accuracy and efficiency of computational formulations. The work of Kiendl et al. [Kiendl et al. \(2009\)](#) is the first combining IGA with rotation-free shells. Since then, rotation-free IGA shells have been steadily advanced, for example to PHT-splines ([Nguyen-Thanh et al., 2011](#)), anisotropic materials ([Nagy et al., 2013](#)), damage ([Deng et al., 2015](#)), biological materials ([Tepole et al., 2015](#)), fracture ([Kiendl et al., 2016](#)), liquid shells ([Sauer et al., 2017](#)), elasto-plasticity ([Ambati et al., 2018](#)), phase separation ([Zimmermann et al., 2019](#)), thermo-mechanical coupling ([Vu-Bac et al., 2019](#)), multi-patch constraints (e.g. see the recent review in Paul et al. [Paul et al. \(2020\)](#)), and reduced quadrature ([Zou et al., 2021](#)). Balabanov et al. [Balabanov et al. \(2019\)](#) present a general strain gradient theory and its corresponding isogeometric finite element formulation for Kirchhoff-Love shells. The formulation requires at least C^2 -continuity of the geometry, but does not account for in-plane fiber bending explicitly.

A formulation for rotation-free isogeometric shells that can capture in-plane bending of embedded fibers has only recently been presented by Schulte et al. [Schulte et al. \(2020\)](#). While the formulation of Schulte et al. is formulated for Kirchhoff-Love shell elements, its underlying theory is based on the strain-gradient theory of Steigmann [Steigmann \(2018\)](#) for shells with embedded rods. In this theory, the strain tensor related to in-plane curvature is of third order, since it expresses the relative change in the surface Christoffel symbols. Strickly speaking, the Christoffel symbols are not tensor components since they do not transform as a tensor. From the material modeling point of view it can thus be inconvenient to formulate invariants of such a strain tensor and interpret their geometrical meaning. Further, the theory of Steigmann [Steigmann \(2018\)](#) and the implementation of Schulte et al. [Schulte et al. \(2020\)](#) are restricted to two fiber families that are initially straight. Another IGA-based finite element formulation for the gradient model of Spencer and Soldatos [Spencer and Soldatos \(2007\)](#) has been presented recently by Witt et al. [Witt et al. \(2021\)](#). However, it is not a shell formulation and it is also restricted to initially straight fibers.

In Duong et al. [Duong et al. \(2021\)](#), we have proposed an advancement that directly extends Kirchhoff-Love shell theory to incorporate general in-plane fiber bending. Although this approach follows the straightforward structure of the classical Kirchhoff-Love shell, the resulting theory has no restriction on the initial state of fibers, the number of fiber families, and also the initial angle between them. Another advantage of the approach is that it directly uses second order surface tensors to characterize the deformation, including in-plane bending, which facilitates the induction of invariants.

In this contribution, we present a rotation-free isogeometric finite element formulation based on the theory by Duong et al. [Duong et al. \(2021\)](#). The proposed formulation can capture anisotropy in stretching, shearing, twisting and bending – both in-plane and out-of-plane. The finite element equations are fully formulated in the curvilinear coordinate system, which avoids the use of local Cartesian coordinate transformations at the element level. In summary, our contribution contains the following novelties and merits:

- It is based on a generalized Kirchhoff-Love shell theory that captures in-plane bending.
- It uses second order tensors for in-plane bending, which facilitates inducing invariants.
- It is analogous to classical rotation-free isogeometric finite shell element formulations.
- It admits initially curved fibers, multiple fiber families and general initial fiber angles.
- It avoids transforming derivatives into Cartesian coordinates at the element level.
- It includes the full linearization and efficient implementation for IGA-based finite elements.

The remaining presentation of the paper is structured as follows: Sec. 2 summarizes the generalized Kirchhoff-Love shell theory of Duong et al. [Duong et al. \(2021\)](#). Sec. 3 presents the

linearization of its weak form and the introduction of the new material tangents associated with in-plane bending. Sec. 4 discusses the finite element discretization of the formulation. Two material models for simple fabrics and woven fabrics are given in Sec. 5. Secs. 6 and 7 illustrate the performance of the proposed formulation by numerical examples with homogeneous and inhomogeneous deformations, respectively. Sec. 8 concludes the paper.

2 Summary of generalized Kirchhoff-Love shell theory

This section summarizes the kinematics, stresses, moments, weak form and constitutive equations according to the generalized thin shell theory of Duong et al. [Duong et al. \(2021\)](#).

2.1 Geometrical description of fiber-embedded surfaces

The mid-surface \mathcal{S} of a thin shell at time t is represented in curvilinear coordinates $(\xi^1, \xi^2) \in \mathcal{P}$ by

$$\mathbf{x} = \mathbf{x}(\xi^\alpha, t), \quad \text{with } \alpha = 1, 2. \quad (1)$$

At any point $\mathbf{x} \in \mathcal{S}$, a curvilinear basis can be constructed from two (covariant) tangent vectors \mathbf{a}_α and a unit normal vector \mathbf{n} to surface \mathcal{S} . They are defined by

$$\mathbf{a}_\alpha := \frac{\partial \mathbf{x}}{\partial \xi^\alpha} = \mathbf{x}_{,\alpha}, \quad \text{and} \quad \mathbf{n} := \frac{\mathbf{a}_1 \times \mathbf{a}_2}{\|\mathbf{a}_1 \times \mathbf{a}_2\|}, \quad (2)$$

where the comma denotes the parametric derivative. The dual tangent vectors \mathbf{a}^α are related to the covariant tangent vectors by $\mathbf{a}_\alpha = a_{\alpha\beta} \mathbf{a}^\beta$ and $\mathbf{a}^\alpha = a^{\alpha\beta} \mathbf{a}_\beta$.⁴ Here, $a_{\alpha\beta} := \mathbf{a}_\alpha \cdot \mathbf{a}_\beta$ and $a^{\alpha\beta} := \mathbf{a}^\alpha \cdot \mathbf{a}^\beta$ denote the surface metrics.

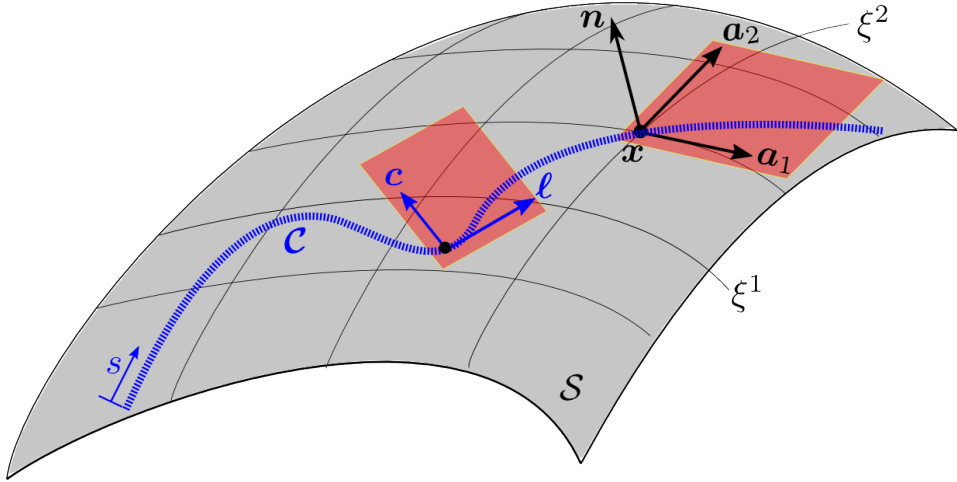


Figure 1: A fiber bundle represented by curve \mathcal{C} embedded in shell surface \mathcal{S} . The red planes illustrate tangent planes ([Duong et al., 2021](#))

Consider a fiber curve (or a curve of fiber bundles) \mathcal{C} embedded in surface \mathcal{S} and given by $\mathbf{x} = \mathbf{x}_\mathcal{C}(s)$ (see Fig. 1). Its normalized tangent vector at location s can be defined by

$$\boldsymbol{\ell} := \frac{\partial \mathbf{x}_\mathcal{C}}{\partial s} = \ell_\alpha \mathbf{a}^\alpha = \ell^\alpha \mathbf{a}_\alpha, \quad (3)$$

⁴Here and henceforth, the summation convention is applied to repeated Greek indices taking values 1 and 2.

while the so-called in-plane fiber director \mathbf{c} , perpendicular to $\boldsymbol{\ell}$, can be defined by

$$\mathbf{c} := \mathbf{n} \times \boldsymbol{\ell} = c_\alpha \mathbf{a}^\alpha = c^\alpha \mathbf{a}_\alpha . \quad (4)$$

The out-of-plane curvature of surface \mathcal{S} can be described by the symmetric second order tensor

$$\mathbf{b} := b_{\alpha\beta} \mathbf{a}^\alpha \otimes \mathbf{a}^\beta , \quad (5)$$

with the components expressed by

$$b_{\alpha\beta} := -\mathbf{n}_{,\alpha} \cdot \mathbf{a}_\beta = \mathbf{n} \cdot \mathbf{a}_{\alpha;\beta} = \mathbf{n} \cdot \mathbf{a}_{\alpha;\beta} . \quad (6)$$

Here,

$$\mathbf{a}_{\alpha;\beta} := \frac{\partial \mathbf{a}_\alpha}{\partial \xi^\beta} = \mathbf{x}_{,\alpha\beta} = \Gamma_{\alpha\beta}^\gamma \mathbf{a}_\gamma + b_{\alpha\beta} \mathbf{n} , \quad \text{and} \quad \mathbf{a}_{\alpha;\beta} := (\mathbf{n} \otimes \mathbf{n}) \mathbf{a}_{\alpha;\beta} \quad (7)$$

are the parametric and covariant derivative of \mathbf{a}_α , respectively. In Eq. (7.1), $\Gamma_{\alpha\beta}^\gamma := \mathbf{a}_{\alpha;\beta} \cdot \mathbf{a}^\gamma$ denote the surface Christoffel symbols. They can be expressed as

$$\Gamma_{\alpha\beta}^\gamma = c^\gamma \Gamma_{\alpha\beta}^c + \ell^\gamma \Gamma_{\alpha\beta}^\ell , \quad (8)$$

where

$$\begin{aligned} \Gamma_{\alpha\beta}^c &:= \mathbf{c} \cdot \mathbf{a}_{\alpha;\beta} = c_\gamma \Gamma_{\alpha\beta}^\gamma , \\ \Gamma_{\alpha\beta}^\ell &:= \boldsymbol{\ell} \cdot \mathbf{a}_{\alpha;\beta} = \ell_\gamma \Gamma_{\alpha\beta}^\gamma . \end{aligned} \quad (9)$$

Furthermore, in order to characterize in-plane curvatures, the so-called in-plane curvature tensor $\bar{\mathbf{b}}$ of fiber \mathcal{C} is defined as the (negative) symmetric part of the projected surface gradient of director \mathbf{c} . That is,

$$\bar{\mathbf{b}} := -\frac{1}{2} [\bar{\nabla}_s \mathbf{c} + (\bar{\nabla}_s \mathbf{c})^T] = \bar{b}_{\alpha\beta} \mathbf{a}^\alpha \otimes \mathbf{a}^\beta , \quad (10)$$

where $\bar{\nabla}_s \bullet := (\bullet_{,\beta} \cdot \mathbf{a}^\alpha) \mathbf{a}_\alpha \otimes \mathbf{a}^\beta$ denotes the projected surface gradient operator.⁵ In Eq. (10), components $\bar{b}_{\alpha\beta}$ can be computed from

$$\bar{b}_{\alpha\beta} = -\frac{1}{2}(c_{\alpha;\beta} + c_{\beta;\alpha}) = -\frac{1}{2}(\mathbf{c}_{,\alpha} \cdot \mathbf{a}_\beta + \mathbf{c}_{,\beta} \cdot \mathbf{a}_\alpha) = -\frac{1}{2}(\bar{\mathbf{c}}_{,\alpha} \cdot \mathbf{a}_\beta + \bar{\mathbf{c}}_{,\beta} \cdot \mathbf{a}_\alpha) , \quad (11)$$

where $\mathbf{c}_{,\alpha} = b_{\alpha\beta} c^\beta \mathbf{n} + c_{;\alpha}^\beta \mathbf{a}_\beta$, and

$$\bar{\mathbf{c}}_{,\alpha} := (\mathbf{a}_\beta \otimes \mathbf{a}^\beta) \mathbf{c}_{,\alpha} = c_{;\alpha}^\beta \mathbf{a}_\beta \quad (12)$$

is the projection of $\mathbf{c}_{,\alpha}$ onto the tangent plane.

2.2 Shell deformation

Shell deformation is measured with respect to the reference configuration \mathcal{S}_0 at time t_0 . Analogous to Sec. 2.1, we define geometrical objects on \mathcal{S}_0 , such as the tangent vectors \mathbf{A}_α , the normal vector \mathbf{N} , the metric $A_{\alpha\beta}$, the out-of-plane curvature tensor $\mathbf{b}_0 := B_{\alpha\beta} \mathbf{A}^\alpha \otimes \mathbf{A}^\beta$, the fiber direction $\mathbf{L} = L^\alpha \mathbf{A}_\alpha = L_\alpha \mathbf{A}^\alpha$, the fiber director $\mathbf{c}_0 = c_\alpha^0 \mathbf{A}^\alpha$, and the in-plane curvature tensor $\bar{\mathbf{b}}_0 := \bar{B}_{\alpha\beta} \mathbf{A}^\alpha \otimes \mathbf{A}^\beta$. The deformation of the fiber-embedded shell can then be characterized by the following quantities:

1. The surface deformation gradient tensor,

$$\mathbf{F} := \mathbf{a}_\alpha \otimes \mathbf{A}^\alpha . \quad (13)$$

⁵ $\bar{\nabla}_s \bullet := \mathbf{i} \nabla_s \bullet$, with $\mathbf{i} = \mathbf{1} - \mathbf{n} \otimes \mathbf{n} = \mathbf{a}_\alpha \otimes \mathbf{a}^\alpha$ and $\nabla_s \bullet = \bullet_{,\alpha} \otimes \mathbf{a}^\alpha$.

It can be used to construct surface strain measures such as the right Cauchy-Green surface tensor $\mathbf{C} := \mathbf{F}^T \mathbf{F} = a_{\alpha\beta} \mathbf{A}^\alpha \otimes \mathbf{A}^\beta$, and the Green-Lagrange surface strain tensor

$$\mathbf{E} := \frac{1}{2}(\mathbf{C} - \mathbf{I}) = \frac{1}{2}(a_{\alpha\beta} - A_{\alpha\beta}) \mathbf{A}^\alpha \otimes \mathbf{A}^\beta = E_{\alpha\beta} \mathbf{A}^\alpha \otimes \mathbf{A}^\beta . \quad (14)$$

2. The *relative out-of-plane curvature tensor*,

$$\mathbf{K} := \mathbf{F}^T \mathbf{b} \mathbf{F} - \mathbf{b}_0 = (b_{\alpha\beta} - B_{\alpha\beta}) \mathbf{A}^\alpha \otimes \mathbf{A}^\beta = K_{\alpha\beta} \mathbf{A}^\alpha \otimes \mathbf{A}^\beta . \quad (15)$$

3. The *relative in-plane curvature tensor*,

$$\bar{\mathbf{K}} := \mathbf{F}^T \bar{\mathbf{b}} \mathbf{F} - \bar{\mathbf{b}}_0 = (\bar{b}_{\alpha\beta} - \bar{B}_{\alpha\beta}) \mathbf{A}^\alpha \otimes \mathbf{A}^\beta = \bar{K}_{\alpha\beta} \mathbf{A}^\alpha \otimes \mathbf{A}^\beta . \quad (16)$$

Remark 2.1: Note, that apart from definition (3.1), the fiber direction vector $\boldsymbol{\ell}$ can also be computed from the (given) reference fiber direction vector \mathbf{L} via the mapping

$$\lambda \boldsymbol{\ell} = \mathbf{F} \mathbf{L} = L^\alpha \mathbf{a}_\alpha , \quad (17)$$

where λ is the fiber stretch. From this and relation (4), one thus obtains

$$\begin{aligned} c_{\beta;\alpha} &= -\ell_\beta (c^\gamma \hat{L}_{\gamma,\alpha} + \ell^\gamma \Gamma_{\gamma\alpha}^c) , \\ c_{;\alpha}^\beta &= -\ell^\beta (c^\gamma \hat{L}_{\gamma,\alpha} + \ell^\gamma \Gamma_{\gamma\alpha}^c) , \end{aligned} \quad (18)$$

on the basis of the definition

$$\hat{L}_{\alpha,\beta} := a_{\alpha\gamma} \hat{L}_{\gamma,\beta}^\gamma , \quad \text{with} \quad \hat{L}_{,\beta}^\alpha := \lambda^{-1} L_{,\beta}^\alpha . \quad (19)$$

Remark 2.2: Inserting (18) into (12) gives

$$\bar{\mathbf{c}}_{,\alpha} = (c^\gamma \hat{L}_{\gamma,\alpha} + \ell^\gamma \Gamma_{\gamma\alpha}^c) \boldsymbol{\ell} . \quad (20)$$

Remark 2.3: The right Cauchy-Green tensor \mathbf{C} and the relative curvature tensors \mathbf{K} and $\bar{\mathbf{K}}$ are all symmetric and of second order. They induce various invariants that can be useful for the constitutive modeling. For example,

$$\begin{aligned} \Lambda &:= \mathbf{C} : \mathbf{L} \otimes \mathbf{L} = a_{\alpha\beta} L^{\alpha\beta} = \lambda^2 , \quad \text{with} \quad L^{\alpha\beta} := L^\alpha L^\beta , \\ K_n &:= \mathbf{K} : \mathbf{L} \otimes \mathbf{L} = (b_{\alpha\beta} - B_{\alpha\beta}) L^{\alpha\beta} , \\ T_g &:= \mathbf{K} : \mathbf{c}_0 \otimes \mathbf{L} = \mathbf{K} : \mathbf{L} \otimes \mathbf{c}_0 = (b_{\alpha\beta} - B_{\alpha\beta}) L^\alpha c_0^\beta , \\ K_g &:= \bar{\mathbf{K}} : \mathbf{L} \otimes \mathbf{L} = (\bar{b}_{\alpha\beta} - \bar{B}_{\alpha\beta}) L^{\alpha\beta} , \end{aligned} \quad (21)$$

express the square of the fiber stretch, the so-called *nominal change in normal curvature*, the *nominal change in geodesic torsion*, and the *nominal change in geodesic curvature* of the curve \mathcal{C} , respectively (see Duong et al. (2021)). It should be noted that the measures K_n , T_g , and K_g are not invariants in a strict sense since their sign is not invariant (although their magnitude still is). Specifically, the sign of K_n and T_g changes when surface director \mathbf{N} is flipped, while the sign of K_g depends on the sign of both \mathbf{N} and \mathbf{L} due to Eqs. (4) and (11).

2.3 Stress and moment tensors

Consider cutting the shell \mathcal{S} virtually apart at $\mathbf{x} \in \mathcal{S}$ by the line $\mathcal{I}(s)$ characterized by the unit tangent vector $\boldsymbol{\tau} := \partial \mathbf{x} / \partial s$ and the unit normal $\boldsymbol{\nu} := \boldsymbol{\tau} \times \mathbf{n} = \nu_\alpha \mathbf{a}^\alpha$. The traction and moment vectors⁶ appearing at the cut are general vectors in \mathbb{R}^3 that can be expressed as

$$\begin{aligned} \mathbf{T} &= T^\alpha \mathbf{a}_\alpha + T^3 \mathbf{n} , \\ \hat{\mathbf{m}} &= m_\tau \boldsymbol{\tau} + m_\nu \boldsymbol{\nu} + \bar{m} \mathbf{n} , \end{aligned} \quad (22)$$

⁶with the units [force/length] and [moment/length] commonly used in shell theory to avoid thickness integration

respectively. The last equation implies that the moment vector $\hat{\mathbf{m}}$ includes a moment $\mathbf{m} := m_\tau \boldsymbol{\tau} + m_\nu \boldsymbol{\nu}$ that causes out-of-plane bending and twisting, and a moment $\bar{\mathbf{m}} := \bar{m} \mathbf{n}$ that causes in-plane bending. The traction and moment vectors (22) induce corresponding internal stresses and moment tensors of the form

$$\begin{aligned}\boldsymbol{\sigma} &= N^{\alpha\beta} \mathbf{a}_\alpha \otimes \mathbf{a}_\beta + S^\alpha \mathbf{a}_\alpha \otimes \mathbf{n} , \\ \hat{\boldsymbol{\mu}} &= m^{\alpha\beta} \mathbf{a}_\alpha \otimes \mathbf{a}_\beta + \bar{m}^\alpha \mathbf{a}_\alpha \otimes \mathbf{n} .\end{aligned}\tag{23}$$

According to Cauchy's theorem, these tensors linearly map the cut normal $\boldsymbol{\nu}$ to the traction and moment vectors (22) as

$$\mathbf{T} = \boldsymbol{\sigma}^\text{T} \boldsymbol{\nu} , \quad \text{and} \quad \hat{\mathbf{m}} = \hat{\boldsymbol{\mu}}^\text{T} \boldsymbol{\nu} .\tag{24}$$

Since moment tensor $\hat{\boldsymbol{\mu}}$ (23.2) is generally asymmetric, it is more convenient to work with the corresponding stress couple tensor instead. To this end, Eq. (24.2) is rewritten as

$$\hat{\mathbf{m}} = \mathbf{m} + \bar{\mathbf{m}} = \mathbf{n} \times \mathbf{M} + \mathbf{c} \times \bar{\mathbf{M}},\tag{25}$$

where

$$\mathbf{M} = \boldsymbol{\mu}^\text{T} \boldsymbol{\nu} , \quad \text{and} \quad \bar{\mathbf{M}} = \bar{\boldsymbol{\mu}}^\text{T} \boldsymbol{\nu} = -\bar{m} \boldsymbol{\ell}\tag{26}$$

denote the so-called stress couple vectors for out-of-plane and in-plane bending, respectively. $\boldsymbol{\mu}$ and $\bar{\boldsymbol{\mu}}$ are the corresponding stress couple tensors. They can be expressed as

$$\boldsymbol{\mu} = -M^{\alpha\beta} \mathbf{a}_\alpha \otimes \mathbf{a}_\beta, \quad \text{and} \quad \bar{\boldsymbol{\mu}} = -\bar{M}^{\alpha\beta} \mathbf{a}_\alpha \otimes \mathbf{a}_\beta .\tag{27}$$

Note that, in order to relate the components of traction and moment vectors to the components of the internal stress and stress couple tensors, one can compare (22) and (24). This gives

$$\begin{aligned}T^\alpha &= \nu_\beta N^{\beta\alpha} , & m_\nu &= M^{\alpha\beta} \nu_\alpha \tau_\beta , \\ T^3 &= \nu_\alpha S^\alpha , & m_\tau &= -M^{\alpha\beta} \nu_\alpha \nu_\beta , \\ \bar{m} &= \bar{M}^{\alpha\beta} \nu_\alpha \ell_\beta = \bar{m}^\alpha \nu_\alpha .\end{aligned}\tag{28}$$

2.4 Weak form and constitutive equations

Consider the shell \mathcal{S} subjected to the external body force $\mathbf{f} = f^\alpha \mathbf{a}_\alpha + p \mathbf{n}$ on \mathcal{S} and to the boundary conditions

$$\mathbf{u} = \bar{\mathbf{u}} \quad \text{on } \partial_u \mathcal{S} , \quad \mathbf{T} = \bar{\mathbf{T}} \quad \text{on } \partial_t \mathcal{S} , \quad \hat{\mathbf{m}} = \bar{\hat{\mathbf{m}}} \quad \text{on } \partial_m \mathcal{S} .\tag{29}$$

Here, $\bar{\mathbf{u}}$ is a prescribed displacement, $\bar{\mathbf{T}}$ is a prescribed boundary traction and $\bar{\hat{\mathbf{m}}}$ is a prescribed bending moment. The equilibrium of the shell is then governed by the balance of linear and angular momentum. Accordingly, the weak form follows as

$$G_{\text{in}} + G_{\text{int}} - G_{\text{ext}} = 0 \quad \forall \delta \mathbf{x} \in \mathcal{V} ,\tag{30}$$

where \mathcal{V} denotes the set of kinematically admissible variations that satisfies boundary condition (29.1), and

$$\begin{aligned}G_{\text{in}} &= \int_{S_0} \delta \mathbf{x} \cdot \rho_0 \dot{\mathbf{v}} \, dA , \\ G_{\text{int}} &= \frac{1}{2} \int_{S_0} \tau^{\alpha\beta} \delta a_{\alpha\beta} \, dA + \int_{S_0} M_0^{\alpha\beta} \delta b_{\alpha\beta} \, dA + \sum_{i=1}^{n_f} \int_{S_0} \bar{M}_{0i}^{\alpha\beta} \delta \bar{b}_{\alpha\beta}^i \, dA , \\ G_{\text{ext}} &= \int_S \delta \mathbf{x} \cdot \mathbf{f} \, da + \int_{\partial S} \delta \mathbf{x} \cdot \mathbf{T} \, ds + \int_{\partial S} \delta \mathbf{n} \cdot \mathbf{M} \, ds + \sum_{i=1}^{n_f} \int_{\partial S} \delta \mathbf{c}_i \cdot \bar{\mathbf{M}}_i \, ds .\end{aligned}\tag{31}$$

Here, n_f denotes the number of fiber families and the quantities indexed by i imply that they are defined for fiber family i . Further, $\tau^{\alpha\beta}$, $M_0^{\alpha\beta}$, and $\bar{M}_{0i}^{\alpha\beta}$ are the components of the nominal effective stress tensor, the nominal stress couple tensor associated with out-of-plane bending, and the nominal stress couple tensor associated with in-plane bending, respectively. They are all symmetric and, for hyperelastic materials, can be obtained as the derivative of a stored energy function,

$$W = W(a_{\alpha\beta}, b_{\alpha\beta}, \bar{b}_{\alpha\beta}^i; h_i^{\alpha\beta}) , \quad (32)$$

with respect to the corresponding work-conjugate kinematic variables defined in Sec. 2.1. That is, the internal virtual work in Eq. (31.2) can be written as $G_{\text{int}} = \int_{S_0} \delta W \, dA$, since

$$\delta W = \frac{1}{2} \tau^{\alpha\beta} \delta a_{\alpha\beta} + M_0^{\alpha\beta} \delta b_{\alpha\beta} + \sum_{i=1}^{n_f} \bar{M}_{0i}^{\alpha\beta} \delta \bar{b}_{\alpha\beta}^i , \quad (33)$$

where

$$\tau^{\alpha\beta} = 2 \frac{\partial W}{\partial a_{\alpha\beta}} , \quad M_0^{\alpha\beta} = \frac{\partial W}{\partial b_{\alpha\beta}} , \quad \bar{M}_{0i}^{\alpha\beta} = \frac{\partial W}{\partial \bar{b}_{\alpha\beta}^i} . \quad (34)$$

In Eq. (32), $h_i^{\alpha\beta}$ collectively denote the components of any structural tensors characterizing material anisotropy. In the following, fiber index i is skipped in $\bar{M}_0^{\alpha\beta}$, $\bar{b}_{\alpha\beta}$, $\hat{L}_{,\alpha}^\beta$, vectors \mathbf{c} , $\boldsymbol{\ell}$, $\bar{\mathbf{m}}$, and $\bar{\mathbf{M}}$ (including their components and derivatives) to simplify the notation where no ambiguities arise.

For G_{int} in Eq. (31.2), one requires the variations (see Duong et al. (2021))

$$\begin{aligned} \delta a_{\alpha\beta} &= \delta \mathbf{a}_\alpha \cdot \mathbf{a}_\beta + \mathbf{a}_\alpha \cdot \delta \mathbf{a}_\beta , \\ \delta b_{\alpha\beta} &= \mathbf{n} \cdot \delta \mathbf{d}_{\alpha\beta} , \quad \text{with} \quad \delta \mathbf{d}_{\alpha\beta} := \delta \mathbf{a}_{\alpha,\beta} - \Gamma_{\alpha\beta}^\gamma \delta \mathbf{a}_\gamma , \\ \bar{M}_0^{\alpha\beta} \delta \bar{b}_{\alpha\beta} &= -\bar{M}_0^{\alpha\beta} (\delta \mathbf{a}_\alpha \cdot \bar{\mathbf{c}}_{,\beta} + \mathbf{a}_\alpha \cdot \delta \bar{\mathbf{c}}_{,\beta}) . \end{aligned} \quad (35)$$

In the last equation, we have used the symmetry of $\bar{M}_0^{\alpha\beta}$.⁷ The variation $\delta \bar{\mathbf{c}}_{,\alpha}$ follows from Eq. (20) as

$$\delta \bar{\mathbf{c}}_{,\alpha} = [\mathcal{L}_\alpha^\gamma (\mathbf{n} \otimes \mathbf{n} + \mathbf{c} \otimes \mathbf{c} - \boldsymbol{\ell} \otimes \boldsymbol{\ell}) - \mathcal{C}_\alpha^\gamma \boldsymbol{\ell} \otimes \mathbf{c} - \mathcal{N}_\alpha^\gamma \boldsymbol{\ell} \otimes \mathbf{n}] \delta \mathbf{a}_\gamma - \ell^\gamma (\boldsymbol{\ell} \otimes \mathbf{c}) \delta \mathbf{a}_{\gamma,\alpha} , \quad (36)$$

where

$$\begin{aligned} \mathcal{L}_\alpha^\gamma &:= -\ell^\gamma (c_\beta \hat{L}_{,\alpha}^\beta + \ell^\beta \Gamma_{\beta\alpha}^c) \\ \mathcal{C}_\alpha^\gamma &:= \hat{L}_{,\alpha}^\gamma - \ell^\gamma (\ell_\beta \hat{L}_{,\alpha}^\beta + \ell^\beta \Gamma_{\beta\alpha}^\ell) \\ \mathcal{N}_\alpha^\gamma &:= c^\gamma \ell^\beta b_{\beta\alpha} . \end{aligned} \quad (37)$$

Further, for the external virtual work (31.3), one requires the variations (see Duong et al. (2021))

$$\begin{aligned} \delta \mathbf{n} &= -(c^\alpha \mathbf{c} \otimes \mathbf{n} + \ell^\alpha \boldsymbol{\ell} \otimes \mathbf{n}) \delta \mathbf{a}_\alpha , \\ \delta \mathbf{c} &= (c^\alpha \mathbf{n} \otimes \mathbf{n} - \ell^\alpha \boldsymbol{\ell} \otimes \mathbf{c}) \delta \mathbf{a}_\alpha . \end{aligned} \quad (38)$$

With this and Eq. (25), the last term in Eq. (31.3) can be rewritten into

$$\int_{\partial S} \delta \mathbf{c} \cdot \bar{\mathbf{M}} \, ds = \int_{\partial S} \delta \mathbf{c} \cdot (\bar{\mathbf{m}} \times \mathbf{c}) \, ds = - \int_{\partial S} \delta \mathbf{c} \cdot \boldsymbol{\ell} \bar{m} \, ds = \int_{\partial S} \ell^\alpha \delta \mathbf{a}_\alpha \cdot \mathbf{c} \bar{m} \, ds , \quad (39)$$

⁷The minus sign in Eq. (35.3) stems from the definition of the in-plane curvature tensor in Eq. (11).

where \bar{m} is an external bending moment causing in-plane bending. Inserting (39) into Eq. (31.3) gives (see also Steigmann (1999); Sauer and Duong (2017))

$$\begin{aligned} G_{\text{ext}} = & \int_{S_0} \delta \mathbf{x} \cdot \mathbf{f}_0 \, dA + \int_S \delta \mathbf{x} \cdot p \mathbf{n} \, da + \int_{\partial_t S} \delta \mathbf{x} \cdot \mathbf{t} \, ds + [\delta \mathbf{x} \cdot m_\nu \mathbf{n}] \\ & + \int_{\partial_{m\tau} S} \delta \mathbf{n} \cdot m_\tau \boldsymbol{\nu} \, ds + \int_{\partial_{\bar{m}} S} \ell^\alpha \delta \mathbf{a}_\alpha \cdot \mathbf{c} \bar{m} \, ds . \end{aligned} \quad (40)$$

Here, we have assumed an external body force of the form $\mathbf{f} = \mathbf{f}_0/J + p \mathbf{n}$, where \mathbf{f}_0 denotes a constant body force, and p is an external pressure acting always normal to shell surface S . Further, $\mathbf{t} := \mathbf{T} - (m_\nu \mathbf{n})'$ is the effective boundary traction, m_τ is external bending moment causing out-of-plane, and m_ν is a point load at corners on Neumann boundaries where $\delta \mathbf{x} \neq \mathbf{0}$.

3 Linearization of the weak form

This section presents the linearization of weak form (30) required for the development of the rotation-free finite element shell formulation in Sec. 4. The more important internal virtual work is discussed here, while the external virtual work can be found in Appendix A.1. We focus on quasi-static conditions, i.e. the inertial term $\rho_0 \dot{\mathbf{v}}$ vanishes.

The linearization of G_{int} in Eq. (31) requires the increment of δW , which follows from Eq. (33) as

$$\begin{aligned} \Delta \delta W = & \delta a_{\alpha\beta} \frac{\partial^2 W}{\partial a_{\alpha\beta} \partial a_{\gamma\delta}} \Delta a_{\gamma\delta} + \delta a_{\alpha\beta} \frac{\partial^2 W}{\partial a_{\alpha\beta} \partial b_{\gamma\delta}} \Delta b_{\gamma\delta} + \frac{\partial W}{\partial a_{\alpha\beta}} \Delta \delta a_{\alpha\beta} \\ & + \delta b_{\alpha\beta} \frac{\partial^2 W}{\partial b_{\alpha\beta} \partial a_{\gamma\delta}} \Delta a_{\gamma\delta} + \delta b_{\alpha\beta} \frac{\partial^2 W}{\partial b_{\alpha\beta} \partial b_{\gamma\delta}} \Delta b_{\gamma\delta} + \frac{\partial W}{\partial b_{\alpha\beta}} \Delta \delta b_{\alpha\beta} \\ & + \sum_{i=1}^{n_f} \left(\delta a_{\alpha\beta} \frac{\partial^2 W}{\partial a_{\alpha\beta} \partial \bar{b}_{\gamma\delta}^i} \Delta \bar{b}_{\gamma\delta}^i + \delta \bar{b}_{\alpha\beta}^i \frac{\partial^2 W}{\partial \bar{b}_{\alpha\beta}^i \partial a_{\gamma\delta}} \Delta a_{\gamma\delta} \right) + \sum_{i,j=1}^{n_f} \left(\delta \bar{b}_{\alpha\beta}^i \frac{\partial^2 W}{\partial \bar{b}_{\alpha\beta}^i \partial \bar{b}_{\gamma\delta}^j} \Delta \bar{b}_{\gamma\delta}^j \right) \\ & + \sum_{i=1}^{n_f} \left(\delta b_{\alpha\beta} \frac{\partial^2 W}{\partial b_{\alpha\beta} \partial \bar{b}_{\gamma\delta}^i} \Delta \bar{b}_{\gamma\delta}^i + \delta \bar{b}_{\alpha\beta}^i \frac{\partial^2 W}{\partial \bar{b}_{\alpha\beta}^i \partial b_{\gamma\delta}} \Delta b_{\gamma\delta} + \frac{\partial W}{\partial \bar{b}_{\alpha\beta}^i} \Delta \delta \bar{b}_{\alpha\beta}^i \right) , \end{aligned} \quad (41)$$

where the term containing indices i and j accounts for an explicit coupling between fiber families. Introducing the material tangents

$$\begin{aligned} c^{\alpha\beta\gamma\delta} &:= 4 \frac{\partial^2 W}{\partial a_{\alpha\beta} \partial a_{\gamma\delta}} = 2 \frac{\partial \tau^{\alpha\beta}}{\partial a_{\gamma\delta}} , & \bar{d}_i^{\alpha\beta\gamma\delta} &:= 2 \frac{\partial^2 W}{\partial a_{\alpha\beta} \partial \bar{b}_{\gamma\delta}^i} = \frac{\partial \tau^{\alpha\beta}}{\partial \bar{b}_{\gamma\delta}^i} , \\ d^{\alpha\beta\gamma\delta} &:= 2 \frac{\partial^2 W}{\partial a_{\alpha\beta} \partial b_{\gamma\delta}} = \frac{\partial \tau^{\alpha\beta}}{\partial b_{\gamma\delta}} , & \bar{e}_i^{\alpha\beta\gamma\delta} &:= 2 \frac{\partial^2 W}{\partial \bar{b}_{\alpha\beta}^i \partial a_{\gamma\delta}} = 2 \frac{\partial \bar{M}_{0i}^{\alpha\beta}}{\partial a_{\gamma\delta}} , \\ e^{\alpha\beta\gamma\delta} &:= 2 \frac{\partial^2 W}{\partial b_{\alpha\beta} \partial a_{\gamma\delta}} = 2 \frac{\partial M_0^{\alpha\beta}}{\partial a_{\gamma\delta}} , & \bar{f}_{ij}^{\alpha\beta\gamma\delta} &:= \frac{\partial^2 W}{\partial \bar{b}_{\alpha\beta}^i \partial \bar{b}_{\gamma\delta}^j} = \frac{\partial \bar{M}_{0i}^{\alpha\beta}}{\partial \bar{b}_{\gamma\delta}^j} , \\ f^{\alpha\beta\gamma\delta} &:= \frac{\partial^2 W}{\partial b_{\alpha\beta} \partial b_{\gamma\delta}} = \frac{\partial M_0^{\alpha\beta}}{\partial b_{\gamma\delta}} , & \bar{g}_i^{\alpha\beta\gamma\delta} &:= \frac{\partial^2 W}{\partial b_{\alpha\beta} \partial \bar{b}_{\gamma\delta}^i} = \frac{\partial M_0^{\alpha\beta}}{\partial \bar{b}_{\gamma\delta}^i} , \\ & & \bar{h}_i^{\alpha\beta\gamma\delta} &:= \frac{\partial^2 W}{\partial \bar{b}_{\alpha\beta}^i \partial b_{\gamma\delta}} = \frac{\partial \bar{M}_{0i}^{\alpha\beta}}{\partial b_{\gamma\delta}} , \end{aligned} \quad (42)$$

Eq. (41) becomes

$$\begin{aligned}
\Delta\delta W = & c^{\alpha\beta\gamma\delta} \frac{1}{2} \delta a_{\alpha\beta} \frac{1}{2} \Delta a_{\gamma\delta} + d^{\alpha\beta\gamma\delta} \frac{1}{2} \delta a_{\alpha\beta} \Delta b_{\gamma\delta} + \tau^{\alpha\beta} \frac{1}{2} \Delta\delta a_{\alpha\beta} \\
& + e^{\alpha\beta\gamma\delta} \delta b_{\alpha\beta} \frac{1}{2} \Delta a_{\gamma\delta} + f^{\alpha\beta\gamma\delta} \delta b_{\alpha\beta} \Delta b_{\gamma\delta} + M_0^{\alpha\beta} \Delta\delta b_{\alpha\beta} \\
& + \sum_{i=1}^{n_f} \left(\bar{d}_i^{\alpha\beta\gamma\delta} \frac{1}{2} \delta a_{\alpha\beta} \Delta \bar{b}_{\gamma\delta}^i + \bar{e}_i^{\alpha\beta\gamma\delta} \delta \bar{b}_{\alpha\beta}^i \frac{1}{2} \Delta a_{\gamma\delta} \right) + \sum_{i,j=1}^{n_f} \left(\bar{f}_{ij}^{\alpha\beta\gamma\delta} \delta \bar{b}_{\alpha\beta}^i \Delta \bar{b}_{\gamma\delta}^j \right) \\
& + \sum_{i=1}^{n_f} \left(\bar{g}_i^{\alpha\beta\gamma\delta} \delta b_{\alpha\beta} \Delta \bar{b}_{\gamma\delta}^i + \bar{h}_i^{\alpha\beta\gamma\delta} \delta \bar{b}_{\alpha\beta}^i \Delta b_{\gamma\delta}^i + \bar{M}_{0i}^{\alpha\beta} \Delta\delta \bar{b}_{\alpha\beta}^i \right) .
\end{aligned} \tag{43}$$

Here and elsewhere, the increments of kinematical quantities like $\Delta a_{\alpha\beta}$, $\Delta b_{\alpha\beta}$, and $\Delta \bar{b}_{\alpha\beta}$ can be taken from their corresponding variations simply by replacing δ with Δ .

Considering the minor symmetries of the material tangents,⁸ we find

$$\begin{aligned}
c^{\alpha\beta\gamma\delta} \frac{1}{2} \delta a_{\alpha\beta} \frac{1}{2} \Delta a_{\gamma\delta} &= \delta \mathbf{a}_\alpha \cdot \mathbf{a}_\beta c^{\alpha\beta\gamma\delta} \mathbf{a}_\gamma \cdot \Delta \mathbf{a}_\delta , \\
d^{\alpha\beta\gamma\delta} \frac{1}{2} \delta a_{\alpha\beta} \Delta b_{\gamma\delta} &= \delta \mathbf{a}_\alpha \cdot \mathbf{a}_\beta d^{\alpha\beta\gamma\delta} \mathbf{n} \cdot \Delta \mathbf{d}_{\gamma\delta} , \\
e^{\alpha\beta\gamma\delta} \delta b_{\alpha\beta} \frac{1}{2} \Delta a_{\gamma\delta} &= \delta \mathbf{d}_{\alpha\beta} \cdot \mathbf{n} e^{\alpha\beta\gamma\delta} \mathbf{a}_\gamma \cdot \Delta \mathbf{a}_\delta , \\
f^{\alpha\beta\gamma\delta} \delta b_{\alpha\beta} \Delta b_{\gamma\delta} &= \delta \mathbf{d}_{\alpha\beta} \cdot \mathbf{n} f^{\alpha\beta\gamma\delta} \mathbf{n} \cdot \Delta \mathbf{d}_{\gamma\delta} , \\
\bar{d}^{\alpha\beta\gamma\delta} \frac{1}{2} \delta a_{\alpha\beta} \Delta \bar{b}_{\gamma\delta} &= \delta \mathbf{a}_\alpha \cdot \mathbf{a}_\beta \bar{d}^{\alpha\beta\gamma\delta} (\mathbf{a}_\delta \cdot \Delta \mathbf{c}_{,\gamma} + \bar{\mathbf{c}}_{,\gamma} \cdot \Delta \mathbf{a}_\delta) , \\
\bar{e}^{\alpha\beta\gamma\delta} \delta \bar{b}_{\alpha\beta} \frac{1}{2} \Delta a_{\gamma\delta} &= (\delta \bar{\mathbf{c}}_{,\alpha} \cdot \mathbf{a}_\beta + \delta \mathbf{a}_\beta \cdot \bar{\mathbf{c}}_{,\alpha}) \bar{e}^{\alpha\beta\gamma\delta} \mathbf{a}_\gamma \cdot \Delta \mathbf{a}_\delta , \\
\bar{f}^{\alpha\beta\gamma\delta} \delta \bar{b}_{\alpha\beta} \Delta \bar{b}_{\gamma\delta} &= (\delta \bar{\mathbf{c}}_{,\alpha} \cdot \mathbf{a}_\beta + \delta \mathbf{a}_\beta \cdot \bar{\mathbf{c}}_{,\alpha}) \bar{f}^{\alpha\beta\gamma\delta} (\mathbf{a}_\delta \cdot \Delta \bar{\mathbf{c}}_{,\gamma} + \bar{\mathbf{c}}_{,\gamma} \cdot \Delta \mathbf{a}_\delta) , \\
\bar{g}^{\alpha\beta\gamma\delta} \delta b_{\alpha\beta} \Delta \bar{b}_{\gamma\delta} &= \delta \mathbf{d}_{\alpha\beta} \cdot \mathbf{n} \bar{g}^{\alpha\beta\gamma\delta} (\mathbf{a}_\delta \cdot \Delta \bar{\mathbf{c}}_{,\gamma} + \bar{\mathbf{c}}_{,\gamma} \cdot \Delta \mathbf{a}_\delta) , \\
\bar{h}^{\alpha\beta\gamma\delta} \delta \bar{b}_{\alpha\beta} \Delta b_{\gamma\delta} &= (\delta \bar{\mathbf{c}}_{,\alpha} \cdot \mathbf{a}_\beta + \delta \mathbf{a}_\beta \cdot \bar{\mathbf{c}}_{,\alpha}) \bar{h}^{\alpha\beta\gamma\delta} \mathbf{n} \cdot \Delta \mathbf{d}_{\gamma\delta} ,
\end{aligned} \tag{44}$$

where Eq. (35) has been used. The linearization of $\delta a_{\alpha\beta}$ and $\delta b_{\alpha\beta}$ follows from Eq. (35.1) and (35.2) as (Sauer and Duong, 2017)

$$\begin{aligned}
\Delta\delta a_{\alpha\beta} &= \delta \mathbf{a}_\alpha \cdot \Delta \mathbf{a}_\beta + \delta \mathbf{a}_\beta \cdot \Delta \mathbf{a}_\alpha , \\
\Delta\delta b_{\alpha\beta} &= -(\delta \mathbf{d}_{\alpha\beta} \cdot \mathbf{a}^\gamma) (\mathbf{n} \cdot \Delta \mathbf{a}_\gamma) - (\delta \mathbf{a}_\gamma \cdot \mathbf{n}) (\mathbf{a}^\gamma \cdot \Delta \mathbf{d}_{\alpha\beta}) - b_{\alpha\beta} a^{\gamma\delta} (\delta \mathbf{a}_\gamma \cdot \mathbf{n}) (\mathbf{n} \cdot \Delta \mathbf{a}_\delta) .
\end{aligned} \tag{45}$$

From Eq. (35.3), we find

$$\bar{M}_0^{\alpha\beta} \Delta\delta \bar{b}_{\alpha\beta} = -\bar{M}_0^{\alpha\beta} (\delta \mathbf{a}_\alpha \cdot \Delta \bar{\mathbf{c}}_{,\beta} + \Delta \mathbf{a}_\alpha \cdot \delta \bar{\mathbf{c}}_{,\beta} + \mathbf{a}_\alpha \cdot \Delta \delta \bar{\mathbf{c}}_{,\beta}) , \tag{46}$$

due to the symmetry of $\bar{M}_0^{\alpha\beta}$. Using Eq. (36), the last term in (46) can be expressed as

$$\bar{M}_0^{\beta\alpha} \mathbf{a}_\beta \cdot \Delta \delta \bar{\mathbf{c}}_{,\alpha} = \delta \mathbf{a}_\gamma \mathbf{P}^{\gamma\beta} \Delta \mathbf{a}_\beta + \delta \mathbf{a}_\beta \mathbf{Q}^{\beta\gamma\alpha} \Delta \mathbf{a}_{\gamma,\alpha} + \delta \mathbf{a}_{\gamma,\alpha} \mathbf{Q}^{\beta\gamma\alpha} \Delta \mathbf{a}_\beta , \tag{47}$$

where we have defined the tensors

$$\begin{aligned}
\mathbf{P}^{\gamma\beta} &:= P_{cc}^{\gamma\beta} \mathbf{c} \otimes \mathbf{c} + P_{\ell\ell}^{\gamma\beta} \boldsymbol{\ell} \otimes \boldsymbol{\ell} + P_{nn}^{\gamma\beta} \mathbf{n} \otimes \mathbf{n} + P_{\ell c}^{\gamma\beta} (\boldsymbol{\ell} \otimes \mathbf{c} + \mathbf{c} \otimes \boldsymbol{\ell}) \\
&+ P_{\ell n}^{\gamma\beta} (\boldsymbol{\ell} \otimes \mathbf{n} + \mathbf{n} \otimes \boldsymbol{\ell}) + P_{nc}^{\gamma\beta} (\mathbf{n} \otimes \mathbf{c} + \mathbf{c} \otimes \mathbf{n}) , \\
\mathbf{Q}^{\beta\gamma\alpha} &:= \ell^{\beta\gamma} \bar{M}_c^\alpha \mathbf{c} \otimes \mathbf{c} - \ell^{\beta\gamma} \bar{M}_\ell^\alpha (\mathbf{c} \otimes \boldsymbol{\ell} + \boldsymbol{\ell} \otimes \mathbf{c}) + c^\beta \ell^\gamma \bar{M}_\ell^\alpha \mathbf{n} \otimes \mathbf{n} .
\end{aligned} \tag{48}$$

⁸I.e. α and β as well as γ and δ can be exchanged in the material tangents.

Here, $\bar{M}_c^\alpha := -\bar{M}_0^{\alpha\beta} c_\beta$, $\bar{M}_\ell^\alpha := -\bar{M}_0^{\alpha\beta} \ell_\beta$, and

$$\begin{aligned}
P_{cc}^{\gamma\beta} &:= \frac{3}{2} \bar{M}_\ell^\alpha (\mathcal{L}_\alpha^\gamma \ell^\beta + \mathcal{L}_\alpha^\beta \ell^\gamma) + \bar{M}_c^\alpha (C_\alpha^\gamma \ell^\beta + C_\alpha^\beta \ell^\gamma) , \\
P_{\ell\ell}^{\gamma\beta} &:= -\bar{M}_\ell^\alpha (\ell^\gamma \mathcal{L}_\alpha^\beta + \ell^\beta \mathcal{L}_\alpha^\gamma) , \\
P_{nn}^{\gamma\beta} &:= \bar{M}_\ell^\alpha C_\alpha^\beta c^\gamma + \bar{M}_\ell^\alpha \mathcal{L}_\alpha^\beta \ell^\gamma - \bar{M}_\ell^\alpha c^\beta \Gamma_{\alpha\delta}^\gamma \ell^\delta - \bar{M}_c^\alpha \mathcal{L}_\alpha^\beta c^\gamma - \bar{M}_0^{\gamma\alpha} \mathcal{L}_\alpha^\beta , \\
P_{\ell c}^{\gamma\beta} &:= -\bar{M}_\ell^\alpha (C_\alpha^\gamma \ell^\beta + \ell^\gamma C_\alpha^\beta) + \bar{M}_c^\alpha (\ell^\gamma \mathcal{L}_\alpha^\beta + \ell^\beta \mathcal{L}_\alpha^\gamma) , \\
P_{\ell n}^{\gamma\beta} &:= -\bar{M}_\ell^\alpha (\mathcal{N}_\alpha^\gamma \ell^\beta + \ell^\gamma \mathcal{N}_\alpha^\beta) , \\
P_{nc}^{\gamma\beta} &:= -\bar{M}_\ell^\alpha b_{\alpha\delta} \ell^\delta (\ell^\gamma \ell^\beta + c^\gamma c^\beta) + \bar{M}_c^\alpha (\mathcal{N}_\alpha^\gamma \ell^\beta + \ell^\gamma \mathcal{N}_\alpha^\beta) ,
\end{aligned} \tag{49}$$

where \mathcal{L}_β^α , C_β^α and \mathcal{N}_β^α are given in Eq. (37).

4 FE discretization

This section presents the finite element discretization and corresponding linearization of weak form (30). An efficient implementation of the FE formulation can then be found in Appendix B.

4.1 Surface discretization

The geometry within an undeformed element Ω_0^e and its deformed counterpart Ω^e is interpolated from the positions of control points \mathbf{X}_e and \mathbf{x}_e , respectively, as

$$\mathbf{X} = \mathbf{N} \mathbf{X}_e , \quad \text{and} \quad \mathbf{x} = \mathbf{N} \mathbf{x}_e , \tag{50}$$

where $\mathbf{N}(\boldsymbol{\xi}) := [N_1 \mathbf{1}, N_2 \mathbf{1}, \dots, N_{n_e} \mathbf{1}]$ is defined based on isogeometric shape functions (Borden et al., 2011) and n_e denotes the number of control points defining the element. From Eq. (50) follows

$$\begin{aligned}
\delta \mathbf{x} &= \mathbf{N} \delta \mathbf{x}_e , \\
\mathbf{a}_\alpha &= \mathbf{N}_{,\alpha} \mathbf{x}_e , \\
\delta \mathbf{a}_\alpha &= \mathbf{N}_{,\alpha} \delta \mathbf{x}_e , \\
\mathbf{a}_{\alpha,\beta} &= \mathbf{N}_{,\alpha\beta} \mathbf{x}_e , \\
\mathbf{a}_{\alpha;\beta} &= \mathbf{N}_{;\alpha\beta} \mathbf{x}_e , \\
\delta \bar{\mathbf{c}}_{,\alpha} &= \mathbf{C}_{,\alpha} \delta \mathbf{x}_e ,
\end{aligned} \tag{51}$$

with

$$\begin{aligned}
\mathbf{N}_{,\alpha} &:= [N_{1,\alpha} \mathbf{1}, N_{2,\alpha} \mathbf{1}, \dots, N_{n_e,\alpha} \mathbf{1}] , \\
\mathbf{N}_{,\alpha\beta} &:= [N_{1,\alpha\beta} \mathbf{1}, N_{2,\alpha\beta} \mathbf{1}, \dots, N_{n_e,\alpha\beta} \mathbf{1}] , \\
\mathbf{N}_{;\alpha\beta} &:= \mathbf{N}_{,\alpha\beta} - \Gamma_{\alpha\beta}^\gamma \mathbf{N}_{,\gamma} , \\
\mathbf{C}_{,\alpha} &:= [\mathcal{L}_\alpha^\gamma (\mathbf{n} \otimes \mathbf{n} + \mathbf{c} \otimes \mathbf{c} - \boldsymbol{\ell} \otimes \boldsymbol{\ell}) - \mathcal{C}_\alpha^\gamma \boldsymbol{\ell} \otimes \mathbf{c} - \mathcal{N}_\alpha^\gamma \boldsymbol{\ell} \otimes \mathbf{n}] \mathbf{N}_{,\gamma} - \ell^\gamma (\boldsymbol{\ell} \otimes \mathbf{c}) \mathbf{N}_{,\gamma\alpha} .
\end{aligned} \tag{52}$$

Here, $N_{A,\alpha} = \partial N_A / \partial \xi^\alpha$, and $N_{A,\alpha\beta} = \partial^2 N_A / (\partial \xi^\alpha \partial \xi^\beta)$ ($A = 1, \dots, n_e$). Further $\mathcal{L}_\alpha^\gamma$, $\mathcal{C}_\alpha^\gamma$, and $\mathcal{N}_\alpha^\gamma$ are defined by Eq. (37). Inserting (51) into (35) gives

$$\begin{aligned} \delta a_{\alpha\beta} &= \delta \mathbf{x}_e^T (\mathbf{N}_{,\alpha}^T \mathbf{N}_{,\beta} + \mathbf{N}_{,\beta}^T \mathbf{N}_{,\alpha}) \mathbf{x}_e , \\ \delta b_{\alpha\beta} &= \delta \mathbf{x}_e^T \mathbf{N}_{;\alpha\beta}^T \mathbf{n} , \\ \bar{M}_0^{\alpha\beta} \delta \bar{b}_{\alpha\beta} &= -\bar{M}_0^{\alpha\beta} (\bar{\mathbf{c}}_{,\beta} \cdot \mathbf{N}_{,\alpha} \delta \mathbf{x}_e + \mathbf{a}_\alpha \cdot \mathbf{C}_{,\beta} \delta \mathbf{x}_e) . \end{aligned} \quad (53)$$

4.2 FE force vectors

Substituting Eqs. (51) and (53) into Eq. (30) gives the discretized weak form

$$\sum_{e=1}^{n_{\text{el}}} (G_{\text{in}}^e + G_{\text{int}}^e - G_{\text{ext}}^e) = \delta \mathbf{x} \cdot \mathbf{f} = 0 \quad \forall \delta \mathbf{x} \in \mathcal{V}^h , \quad (54)$$

where n_{el} is the number of elements, \mathbf{f} denotes the global FE force vector, and \mathcal{V}^h denotes the set of kinematically admissible variations for the control points.

In order to obtain the virtual work of the internal FE forces, we insert interpolation (53) into Eq. (31.2). This gives

$$G_{\text{int}}^e = \delta \mathbf{x}_e^T (\mathbf{f}_{\text{int}\tau}^e + \mathbf{f}_{\text{int}M}^e + \mathbf{f}_{\text{int}\bar{M}}^e) , \quad (55)$$

where

$$\begin{aligned} \mathbf{f}_{\text{int}\tau}^e &:= \int_{\Omega_0^e} \tau^{\alpha\beta} \mathbf{N}_{,\alpha}^T \mathbf{a}_\beta \, dA , \\ \mathbf{f}_{\text{int}M}^e &:= \int_{\Omega_0^e} M_0^{\alpha\beta} \mathbf{N}_{;\alpha\beta}^T \mathbf{n} \, dA , \\ \mathbf{f}_{\text{int}\bar{M}}^e &:= - \int_{\Omega_0^e} \bar{M}_0^{\alpha\beta} (\mathbf{N}_{,\alpha}^T \bar{\mathbf{c}}_{,\beta} + \mathbf{C}_{,\beta}^T \mathbf{a}_\alpha) \, dA . \end{aligned} \quad (56)$$

Discretization of the external virtual work in Eq. (40) gives, see Eq. (39) and also Sauer et al. (2014); Sauer and Duong (2017)

$$G_{\text{ext}}^e = \delta \mathbf{x}_e^T (\mathbf{f}_{\text{ext}0}^e + \mathbf{f}_{\text{ext}p}^e + \mathbf{f}_{\text{ext}t}^e + \mathbf{f}_{\text{ext}m}^e + \mathbf{f}_{\text{ext}\bar{m}}^e) + \delta \mathbf{x}_A \cdot \mathbf{f}_{\text{ext}m_\nu}^A , \quad (57)$$

where

$$\begin{aligned} \mathbf{f}_{\text{ext}0}^e &:= \int_{\Omega_0^e} \mathbf{N}^T \mathbf{f}_0 \, dA , \\ \mathbf{f}_{\text{ext}p}^e &:= \int_{\Omega^e} \mathbf{N}^T p \mathbf{n} \, da , \\ \mathbf{f}_{\text{ext}t}^e &:= \int_{\partial_t \Omega^e} \mathbf{N}^T \mathbf{t} \, ds , \\ \mathbf{f}_{\text{ext}m_\tau}^e &:= - \int_{\partial_{m\tau} \Omega^e} \mathbf{N}_{,\alpha}^T \nu^\alpha m_\tau \mathbf{n} \, ds , \\ \mathbf{f}_{\text{ext}\bar{m}}^e &:= \int_{\partial_{\bar{m}} \Omega^e} \mathbf{N}_{,\alpha}^T \ell^\alpha \bar{m} \mathbf{c} \, ds , \\ \mathbf{f}_{\text{ext}m_\nu}^A &:= m_\nu \mathbf{n}_A \end{aligned} \quad (58)$$

are the external FE force vectors. Here, $\mathbf{f}_{\text{ext}m_\nu}^A$ is a possible corner force at corner node \mathbf{x}_A due to a twisting moment m_ν applied on a non-smooth boundary (cf. Sauer and Duong (2017), Sec. 6.3).

4.3 Tangent matrices

The tangent matrices associated with the internal and external FE forces in (56) and (58) are derived as follows.

4.3.1 Tangent matrices of the internal FE forces

The internal tangent matrices can be found by linearizing (55). This gives

$$\Delta G_{\text{int}}^e = \delta \mathbf{x}_e^T (\mathbf{k}_{\text{mat}}^e + \mathbf{k}_{\text{geo}}^e) \Delta \mathbf{x}_e , \quad (59)$$

where \mathbf{k}_{mat} denotes the material tangent

$$\mathbf{k}_{\text{mat}}^e = \mathbf{k}_{\tau\tau}^e + \mathbf{k}_{\tau M}^e + \mathbf{k}_{M\tau}^e + \mathbf{k}_{MM}^e + \mathbf{k}_{\tau\bar{M}}^e + \mathbf{k}_{\bar{M}\tau}^e + \mathbf{k}_{\bar{M}\bar{M}}^e + \mathbf{k}_{M\bar{M}}^e + \mathbf{k}_{\bar{M}M}^e , \quad (60)$$

with

$$\begin{aligned} \mathbf{k}_{\tau\tau}^e &:= \int_{\Omega_0^e} c^{\alpha\beta\gamma\delta} \mathbf{N}_{,\alpha}^T (\mathbf{a}_\beta \otimes \mathbf{a}_\gamma) \mathbf{N}_{,\delta} dA , \\ \mathbf{k}_{\tau M}^e &:= \int_{\Omega_0^e} d^{\alpha\beta\gamma\delta} \mathbf{N}_{,\alpha}^T (\mathbf{a}_\beta \otimes \mathbf{n}) \mathbf{N}_{,\gamma\delta} dA , \\ \mathbf{k}_{M\tau}^e &:= \int_{\Omega_0^e} e^{\alpha\beta\gamma\delta} \mathbf{N}_{;\alpha\beta}^T (\mathbf{n} \otimes \mathbf{a}_\gamma) \mathbf{N}_{,\delta} dA , \\ \mathbf{k}_{MM}^e &:= \int_{\Omega_0^e} f^{\alpha\beta\gamma\delta} \mathbf{N}_{;\alpha\beta}^T (\mathbf{n} \otimes \mathbf{n}) \mathbf{N}_{;\gamma\delta} dA , \\ \mathbf{k}_{\tau\bar{M}}^e &:= \int_{\Omega_0^e} \bar{d}^{\alpha\beta\gamma\delta} \mathbf{N}_{,\alpha}^T \mathbf{a}_\beta \otimes (\mathbf{a}_\delta \mathbf{C}_{,\gamma} + \bar{\mathbf{c}}_{,\gamma} \mathbf{N}_{,\delta}) dA , \\ \mathbf{k}_{\bar{M}\tau}^e &:= \int_{\Omega_0^e} \bar{e}^{\alpha\beta\gamma\delta} (\mathbf{C}_{,\alpha}^T \mathbf{a}_\beta + \mathbf{N}_{,\beta}^T \bar{\mathbf{c}}_{,\alpha}) \otimes \mathbf{a}_\gamma \mathbf{N}_{,\delta} dA , \\ \mathbf{k}_{\bar{M}\bar{M}}^e &:= \int_{\Omega_0^e} \bar{f}^{\alpha\beta\gamma\delta} (\mathbf{C}_{,\alpha}^T \mathbf{a}_\beta + \mathbf{N}_{,\beta}^T \bar{\mathbf{c}}_{,\alpha}) \otimes (\mathbf{a}_\delta \mathbf{C}_{,\gamma} + \bar{\mathbf{c}}_{,\gamma} \mathbf{N}_{,\delta}) dA , \\ \mathbf{k}_{M\bar{M}}^e &:= \int_{\Omega_0^e} \bar{g}^{\alpha\beta\gamma\delta} \mathbf{N}_{;\alpha\beta}^T \mathbf{n} \otimes (\mathbf{a}_\delta \mathbf{C}_{,\gamma} + \bar{\mathbf{c}}_{,\gamma} \mathbf{N}_{,\delta}) dA , \\ \mathbf{k}_{\bar{M}M}^e &:= \int_{\Omega_0^e} \bar{h}^{\alpha\beta\gamma\delta} (\mathbf{C}_{,\alpha}^T \mathbf{a}_\beta + \mathbf{N}_{,\beta}^T \bar{\mathbf{c}}_{,\alpha}) \otimes \mathbf{n} \mathbf{N}_{;\gamma\delta} dA , \end{aligned} \quad (61)$$

while $\mathbf{k}_{\text{geo}}^e$ denotes the geometrical tangent

$$\mathbf{k}_{\text{geo}}^e = \mathbf{k}_\tau^e + \mathbf{k}_M^e + \mathbf{k}_{\bar{M}}^e , \quad (62)$$

with

$$\begin{aligned} \mathbf{k}_\tau^e &= + \int_{\Omega_0^e} \tau^{\alpha\beta} \mathbf{N}_{,\alpha}^T \mathbf{N}_{,\beta} dA , \\ \mathbf{k}_M^e &= - \int_{\Omega_0^e} M_0^{\alpha\beta} [\mathbf{N}_{,\gamma}^T (\mathbf{n} \otimes \mathbf{a}^\gamma) \mathbf{N}_{;\alpha\beta} + \mathbf{N}_{;\alpha\beta}^T (\mathbf{a}^\gamma \otimes \mathbf{n}) \mathbf{N}_{,\gamma}] dA \\ &\quad - \int_{\Omega_0^e} (b_{\alpha\beta} M_0^{\alpha\beta}) a^{\gamma\delta} \mathbf{N}_{,\gamma}^T (\mathbf{n} \otimes \mathbf{n}) \mathbf{N}_{,\delta} dA , \end{aligned} \quad (63)$$

and

$$\begin{aligned} \mathbf{k}_{\bar{M}}^e &= - \int_{\Omega_0^e} \bar{M}_0^{\alpha\beta} (\mathbf{N}_{,\alpha}^T \mathbf{C}_{,\beta} + \mathbf{C}_{,\beta}^T \mathbf{N}_{,\alpha}) dA - \int_{\Omega_0^e} \mathbf{N}_{,\gamma}^T \mathbf{P}^{\gamma\beta} \mathbf{N}_{,\beta} dA \\ &\quad - \int_{\Omega_0^e} (\mathbf{N}_{,\beta}^T \mathbf{Q}^{\beta\gamma\alpha} \mathbf{N}_{,\gamma\alpha} + \mathbf{N}_{,\gamma\alpha}^T \mathbf{Q}^{\beta\gamma\alpha} \mathbf{N}_{,\beta}) dA , \end{aligned} \quad (64)$$

where $\mathbf{P}^{\gamma\beta}$ and $\mathbf{Q}^{\gamma\beta\alpha}$ are defined by Eq. (49). As expected, $\mathbf{k}_{\text{mat}}^e$ and $\mathbf{k}_{\text{geo}}^e$ are symmetric.

Remark 4.1: As seen in Eq. (61) and (62), in-plane bending in general adds five material tangents (the last five terms in (61)) and one geometrical tangent, (64), to the rotation-free shell formulation of Duong et al. [Duong et al. \(2017\)](#).

4.3.2 Tangent matrices of the external FE forces

By linearizing and rearranging (57), one obtains

$$\Delta G_{\text{ext}}^e = \delta \mathbf{x}_e^T \mathbf{k}_{\text{ext}}^e \Delta \mathbf{x}_e + \delta \mathbf{x}_A^T \mathbf{k}_{\text{ext}m_\nu}^A \Delta \mathbf{x}_A, \quad (65)$$

which contains the external tangent matrices

$$\mathbf{k}_{\text{ext}}^e := \mathbf{k}_{\text{ext}p}^e + \mathbf{k}_{\text{ext}t}^e + \mathbf{k}_{\text{ext}m_\tau}^e + \mathbf{k}_{\text{ext}\bar{m}}^e. \quad (66)$$

Here, $\mathbf{k}_{\text{ext}p}^e$, $\mathbf{k}_{\text{ext}t}^e$, $\mathbf{k}_{\text{ext}m_\tau}^e$, $\mathbf{k}_{\text{ext}\bar{m}}^e$, and $\mathbf{k}_{\text{ext}m_\nu}^A$ are the tangent matrices associated with $\mathbf{f}_{\text{ext}p}^e$, $\mathbf{f}_{\text{ext}t}^e$, $\mathbf{f}_{\text{ext}m}^e$, $\mathbf{f}_{\text{ext}\bar{m}}^e$, and $\mathbf{f}_{\text{ext}m_\nu}^A$ defined in Eq. (58), respectively. Their expressions are given in Appendix A.2.

5 Material model examples

This section presents two hyperelastic phenomenological material models for fabrics. The first is a simple fabric model – motivated by numerical convenience – that can be used to test numerical aspects of the proposed finite shell element formulation. The second is a physically-based model for (plainly) woven fabrics.

Since inducing invariants for the new in-plane curvature tensor $\bar{\mathbf{K}}$ is very similar to inducing invariants for the out-of-plane curvature tensor \mathbf{K} , the construction of material models for the proposed shell formulation can follow that of classical shells. Further, as in the FE formulation of Duong et al. [Duong et al. \(2017\)](#), the proposed shell formulation can admit material models expressed directly in terms of the invariants of the surface tensors such as is considered here. The unit of the strain energy density W is thus energy per reference area. This approach facilitates efficient simulations since through-the-thickness integration is not required.⁹ However, our proposed shell formulation can also incorporate material models that are extracted from 3D continua by (numerical) integration over the thickness, see Duong et al. [Duong et al. \(2017\)](#).

5.1 A simple fabric model

We consider a general fabric consisting of n_f fiber families that can be initially curved and possibly bonded to a matrix. We assume that the total strain energy function W can be additively decomposed into the strain energies of the matrix deformation W_{matrix} , fiber stretching $W_{\text{fib-stretch}}$, out-of-plane and in-plane fiber bending $W_{\text{fib-bending}}$, fiber torsion $W_{\text{fib-torsion}}$, and the linkage between fiber families $W_{\text{fib-angle}}$. That is,

$$W = W_{\text{matrix}} + W_{\text{fib-stretch}} + W_{\text{fib-bending}} + W_{\text{fib-torsion}} + W_{\text{fib-angle}}. \quad (67)$$

⁹This does not imply that the thickness is neglected, instead its influence is embedded in the model.

A simple material model is given by

$$\begin{aligned}
W_{\text{matrix}} &= U(J) + \frac{1}{2}\mu (I_1 - 2 - 2 \ln J) , \\
W_{\text{fib-stretch}} &= \frac{1}{8} \sum_{i=1}^{n_f} \epsilon_L^i (\Lambda_i - 1)^2 , \\
W_{\text{fib-bending}} &= \frac{1}{2} \sum_{i=1}^{n_f} \left[\beta_n^i (K_n^i)^2 + \beta_g^i (K_g^i)^2 \right] , \\
W_{\text{fib-torsion}} &= \frac{1}{2} \sum_{i=1}^{n_f} \beta_\tau^i (T_g^i)^2 , \\
W_{\text{fib-angle}} &= \frac{1}{4} \sum_{i=1}^{n_f-1} \sum_{j=i+1}^{n_f} \epsilon_a^{ij} (\gamma_{ij} - \gamma_{ij}^0)^2 ,
\end{aligned} \tag{68}$$

where $U(J)$ is the surface dilatation energy, and where Λ_i , T_g^i , K_n^i , and K_g^i are defined in Eq. (21) for fiber family i . Further, $\gamma_{ij} := \mathbf{C} : \mathbf{L}_i \otimes \mathbf{L}_j$ and $\gamma_{ij}^0 := \mathbf{L}_i \cdot \mathbf{L}_j$ describe the angle between fiber families i and j in the current and reference configuration, respectively. Parameters μ , ϵ_L^i , ϵ_a^{ij} , β_n^i , β_g^i , and β_τ^i denote material constants. The effective stress and moment components follows from Eq. (67) and (68) as

$$\begin{aligned}
\tau^{\alpha\beta} &= \tau_{\text{matrix}}^{\alpha\beta} + \frac{1}{2} \sum_{i=1}^{n_f} \epsilon_L^i (\Lambda_i - 1) L_i^{\alpha\beta} + \sum_{i=1}^{n_f-1} \sum_{j=i+1}^{n_f} \epsilon_a^{ij} (\gamma_{ij} - \gamma_{ij}^0) (L_i^\alpha L_j^\beta)^{\text{sym}} , \\
M_0^{\alpha\beta} &= \sum_{i=1}^{n_f} \beta_n^i K_n^i L_i^{\alpha\beta} + \sum_{i=1}^{n_f} \beta_\tau^i T_g^i (c_{0i}^\alpha L_i^\beta)^{\text{sym}} , \\
\bar{M}_0^{\alpha\beta} &= \sum_{i=1}^{n_f} \beta_g^i K_g^i L_i^{\alpha\beta} ,
\end{aligned} \tag{69}$$

where $\tau_{\text{matrix}}^{\alpha\beta} = J U' a^{\alpha\beta} + \mu (A^{\alpha\beta} - a^{\alpha\beta})$ is the stress due to the matrix response, and where $(\bullet^{\alpha\beta})^{\text{sym}} = (\bullet^{\alpha\beta} + \bullet^{\beta\alpha})/2$ denotes symmetrization. Further, the material tangents of (69) follow from Eq. (42) as

$$\begin{aligned}
c^{\alpha\beta\gamma\delta} &= c_{\text{matrix}}^{\alpha\beta\gamma\delta} + \sum_{i=1}^{n_f} \epsilon_L^i L_i^{\alpha\beta} L_i^{\gamma\delta} + 2 \sum_{i=1}^{n_f-1} \sum_{j=i+1}^{n_f} \epsilon_a^{ij} (L_i^\alpha L_j^\beta)^{\text{sym}} (L_i^\gamma L_j^\delta)^{\text{sym}} , \\
f^{\alpha\beta\gamma\delta} &= \sum_{i=1}^{n_f} \beta_n^i L_i^{\alpha\beta} L_i^{\gamma\delta} + \sum_{i=1}^{n_f} \beta_\tau^i (c_{0i}^\alpha L_i^\beta)^{\text{sym}} (c_{0i}^\gamma L_i^\delta)^{\text{sym}} , \\
\bar{f}_i^{\alpha\beta\gamma\delta} &= \sum_{i=1}^{n_f} \beta_g^i L_i^{\alpha\beta} L_i^{\gamma\delta} , \\
d^{\alpha\beta\gamma\delta} &= e^{\alpha\beta\gamma\delta} = \bar{d}_i^{\alpha\beta\gamma\delta} = \bar{e}_i^{\alpha\beta\gamma\delta} = \bar{g}_i^{\alpha\beta\gamma\delta} = \bar{h}_i^{\alpha\beta\gamma\delta} = 0 ,
\end{aligned} \tag{70}$$

with

$$c_{\text{matrix}}^{\alpha\beta\gamma\delta} = -(J U' - \mu) (a^{\alpha\gamma} a^{\beta\delta} + a^{\alpha\delta} a^{\beta\gamma}) + J(U' + J U'') a^{\alpha\beta} a^{\gamma\delta} . \tag{71}$$

5.2 A woven fabric model

In this section, a physically-based hyperelastic material model of dry woven fabrics is proposed.¹⁰ We consider plain weave fabrics with two fiber families. The model will be fitted to the experiment data provided by Cao et al. [Cao et al. \(2008\)](#).

For simplification, we assume that fibers embedded in the apparent textile surface are nearly inextensible in the averaged fiber direction ℓ_i .¹¹ We further assume that fibers in the fabrics are perfectly bonded to each other (i.e. without inter-fiber sliding), such that hyperelasticity can be assumed. Accordingly, we propose a strain energy of the form

$$W = W_{\text{fib-stretch}} + W_{\text{fib-bending}} + W_{\text{fib-angle}} , \quad (72)$$

with

$$\begin{aligned} W_{\text{fib-stretch}} &= \frac{1}{2} \sum_{i=1}^2 \epsilon_L^i (\lambda_i - 1)^2 , \\ W_{\text{fib-bending}} &= \frac{1}{2} \sum_{i=1}^2 \beta_g^i (K_g^i)^2 , \\ W_{\text{fib-angle}} &= \frac{\mu}{2} \left(\hat{\gamma} \operatorname{asinh}(\alpha_1 \hat{\gamma}) - \frac{1}{\alpha_1} \sqrt{\alpha_1^2 \hat{\gamma}^2 + 1} \right) + \frac{\eta}{2\alpha_2} \cosh(\alpha_2 \hat{\gamma}) , \end{aligned} \quad (73)$$

where K_g^i is defined in Eq. (21.4) for fiber family i , and $\hat{\gamma} := \ell_1 \cdot \ell_2$ describes the fiber angle between fiber family 1 and 2. Further, ϵ_L^i , β_g^i , μ , α_1 , α_2 , and η are material parameters (see Tab. 1). The choice of $W_{\text{fib-angle}}$ in Eq. (73) is motivated both physically (i.e. to reproduce the shear response observed experimentally) and numerically (i.e. to get a well-behaved and smooth tangent matrix). The two shearing energy terms in Eq. (73.3) phenomenologically reflect two assumed mechanisms of bonding between yarns of the two fiber families. The first one is due to friction between yarns dominating at small deformations, and the second is due to geometrical interlocking of yarns at large deformations (or *yarn-yarn lock-up* ([Cao et al., 2008](#))).

Parameter	value	unit	physical meaning
ϵ_L^i	50	N/mm	tensile stiffness of fiber family i
β_g^i	4.8	N mm	in-plane bending stiffness of fiber family i
μ	1.6	mN/mm	initial shear modulus due to yarn-yarn friction
α_1	305	-	plateau parameter of yarn-yarn friction
η	2.0	mN/mm	shear modulus due to geometrical yarn-yarn interlocking
α_2	5.4215	-	plateau parameter of geometrical yarn-yarn interlocking

Table 1: Material parameters for material model (73). The values are obtained from fitting (73) to the experimental data of the bias extension test for sample #1 of Cao et al. [Cao et al. \(2008\)](#), see Sec. 7.1.1.

Following from (72) and (73), the effective stress and moment components become

$$\begin{aligned} \tau^{\alpha\beta} &= \sum_{i=1}^2 \epsilon_L^i (\lambda_i - 1) \frac{1}{\lambda_i} L_i^{\alpha\beta} + S l_{12}^{\alpha\beta} , \\ \bar{M}_0^{\alpha\beta} &= \sum_{i=1}^2 \beta_g^i K_g^i L_i^{\alpha\beta} , \end{aligned} \quad (74)$$

¹⁰Dry fabrics are fabrics that are not embedded within a matrix material.

¹¹Due to initial crimping, fibers are not straight initially and hence may appear extensible.

where we have defined $S(\hat{\gamma}) := \mu \operatorname{asinh}(\alpha_1 \hat{\gamma}) + \eta \operatorname{sinh}(\alpha_2 \hat{\gamma})$, and

$$l_{12}^{\alpha\beta} := (\ell_1^\alpha \ell_2^\beta)^{\operatorname{sym}} - \frac{\hat{\gamma}}{2} (\ell_1^{\alpha\beta} + \ell_2^{\alpha\beta}) . \quad (75)$$

By applying Eq. (42) to material model (72), we further find the material tangents as

$$\begin{aligned} c^{\alpha\beta\gamma\delta} &= \sum_{i=1}^2 \epsilon_L^i \frac{1}{\lambda_i} \ell_i^{\alpha\beta} \ell_i^{\gamma\delta} + 2 S l_{12}^{\alpha\beta\gamma\delta} + 2 S' l_{12}^{\alpha\beta} l_{12}^{\gamma\delta} , \\ \bar{f}^{\alpha\beta\gamma\delta} &= \sum_{i=1}^2 \beta_g^i L_i^{\alpha\beta} L_i^{\gamma\delta} , \\ d^{\alpha\beta\gamma\delta} &= e^{\alpha\beta\gamma\delta} = f^{\alpha\beta\gamma\delta} = g^{\alpha\beta\gamma\delta} = h^{\alpha\beta\gamma\delta} = \bar{h}^{\alpha\beta\gamma\delta} = \bar{e}^{\alpha\beta\gamma\delta} = 0 , \end{aligned} \quad (76)$$

where $S' = \mu \alpha_1 (1/\sqrt{\alpha_1^2 \hat{\gamma}^2 + 1}) + \eta \alpha_2 \cosh(\alpha_2 \hat{\gamma})$, and

$$l_{12}^{\alpha\beta\gamma\delta} := \frac{\partial l_{12}^{\alpha\beta}}{\partial a_{\gamma\delta}} = -(\ell_1^\alpha \ell_2^\beta)^{\operatorname{sym}} \frac{1}{2} (\ell_1^{\gamma\delta} + \ell_2^{\gamma\delta}) - \frac{1}{2} (\ell_1^{\alpha\beta} + \ell_2^{\alpha\beta}) l_{12}^{\gamma\delta} + \frac{\hat{\gamma}}{2} (\ell_1^{\alpha\beta} \ell_1^{\gamma\delta} + \ell_2^{\alpha\beta} \ell_2^{\gamma\delta}) . \quad (77)$$

5.3 An effective (stabilized) fiber compression model

In most textile materials, fibers buckle under axial compression. If the buckling is microscopic,¹² the fibers macroscopically appear to have much smaller stiffness in compression than in tension. For simplification, the (microscopic) buckling is usually not simulated explicitly and the compressive stiffness is usually neglected in the construction of material models. For instance, one can simply set $\epsilon_L^i = 0$ for $\lambda_i < 1$ in material models (68) and (73).

Although the latter simplification does not affect the accuracy much, it can still lead to a material instability¹³ in quasi-static computations. Therefore, if no other medium, e.g. matrix, effectively supports the fibers, a stabilization technique may be necessary. For this purpose, we consider the additional stabilization term

$$W_{\text{fib-stab}} = \frac{1}{2} \epsilon_{\text{stab}}^e \sum_{i=1}^{n_f} (\lambda_i - 1)^2 + \frac{1}{2} \epsilon_{\text{stab}}^v \sum_{i=1}^{n_f} (\tilde{\lambda}_i - 1)^2 \quad (78)$$

in the strain energy in case $\lambda_i < 1$. Here, ϵ_{stab}^e and ϵ_{stab}^v are stabilization parameters, and

$$\tilde{\lambda}_i^2 := a_{\alpha\beta} \ell_{i\text{-pre}}^{\alpha\beta} = \frac{a_{\alpha\beta} L_i^{\alpha\beta}}{a_{\gamma\delta}^{\text{pre}} L_i^{\gamma\delta}} \quad (79)$$

denotes the instantaneous fiber stretch measured with respect to the configuration at the preceding computational load or time step. Term (78) leads to the stabilization stress

$$\tau_{\text{fib-stab}}^{\alpha\beta} = \epsilon_{\text{stab}}^e \sum_{i=1}^{n_f} (\lambda_i - 1) \frac{1}{\lambda_i} L_i^{\alpha\beta} + \epsilon_{\text{stab}}^v \sum_{i=1}^{n_f} (\tilde{\lambda}_i - 1) \frac{1}{\tilde{\lambda}_i} \ell_{i\text{-pre}}^{\alpha\beta} \quad (80)$$

and its tangent

$$c_{\text{fib-stab}}^{\alpha\beta\gamma\delta} = \epsilon_{\text{stab}}^e \sum_{i=1}^{n_f} \lambda_i^{-3} L_i^{\alpha\beta} L_i^{\gamma\delta} + \epsilon_{\text{stab}}^v \sum_{i=1}^{n_f} \tilde{\lambda}_i^{-3} \ell_{i\text{-pre}}^{\alpha\beta} \ell_{i\text{-pre}}^{\gamma\delta} . \quad (81)$$

¹²I.e. at the length scale of a single fiber.

¹³I.e. a instability due to a lack of stiffness in a particular direction at a material point.

Remark 5.1: Note that the stress in Eq. (80) (and its tangent in Eq. (81)) are added into the system only for fiber compression, i.e. $\lambda_i < 1$.

Remark 5.2: The first term in (78) corresponds to the elasticity of fibers (or a bundle of fibers) in compression. In some cases, this compressive resistance can be physically justified. E.g. for woven fabrics, a small resistance stems from the small local out-of-plane fiber bending stiffness due to initial crimping of yarns in the fabrics. On the other hand, the first term in Eq. (78) can also be used as a penalty regularization for enforcing near incompressibility of fibers (if required), by simply setting ϵ_{stab}^e to a large value.

Remark 5.3: The second term in (78) provides numerical damping to fibers in compression. It stems from the potential

$$W_v^i := \frac{1}{2} \eta (\dot{\tilde{\lambda}}_i)^2, \quad (82)$$

where η denotes the so-called (instantaneous) stretching viscosity, and the approximation $\dot{\tilde{\lambda}}_i \approx (\tilde{\lambda}_i - 1)/\Delta t$, with Δt being time step size, has been used. Therefore, ϵ_{stab}^v relates to the stretching viscosity by $\eta := 2 \epsilon_{\text{stab}}^v \Delta t^2$.

Remark 5.4: The second term in (78) is influenced not only by the parameter ϵ_{stab}^v but also depends upon step size Δt . That is, for a fixed ϵ_{stab}^v , the stretch $\tilde{\lambda}_i$ approaches 1 when Δt decreases. Hence, the stored energy $\epsilon_{\text{stab}}^v (\tilde{\lambda}_i - 1)^2$ consistently approaches zero as $\Delta t \rightarrow 0$.

6 Numerical examples: Homogeneous deformation

This section verifies the proposed finite element shell formulation via several benchmark examples characterized by homogeneous deformations. The FE simulation results are compared with exact solutions provided by Duong et al. [Duong et al. \(2021\)](#). For all these examples, the domain is discretized by a single quadratic NURBS patch. Material model (67)–(68) is used, with its parameters specified separately for each example.

For unit normalization, we use a reference length L_0 , and a reference surface stress ϵ_0 , which has the unit [force/length]. Therefore, the unit of surface strain energy density W , reaction forces, and reaction moments is $[\epsilon_0]$, $[\epsilon_0 L_0]$, and $[\epsilon_0 L_0^2]$, respectively. The units of the material parameters in model (67)–(68) then follow as: $[\epsilon_0]$ for meambrane stiffnesses μ , ϵ_L , ϵ_a , and $[\epsilon_0 L_0^2]$ for bending stiffnesses β_n , β_τ , β_g .

6.1 Uniaxial tension

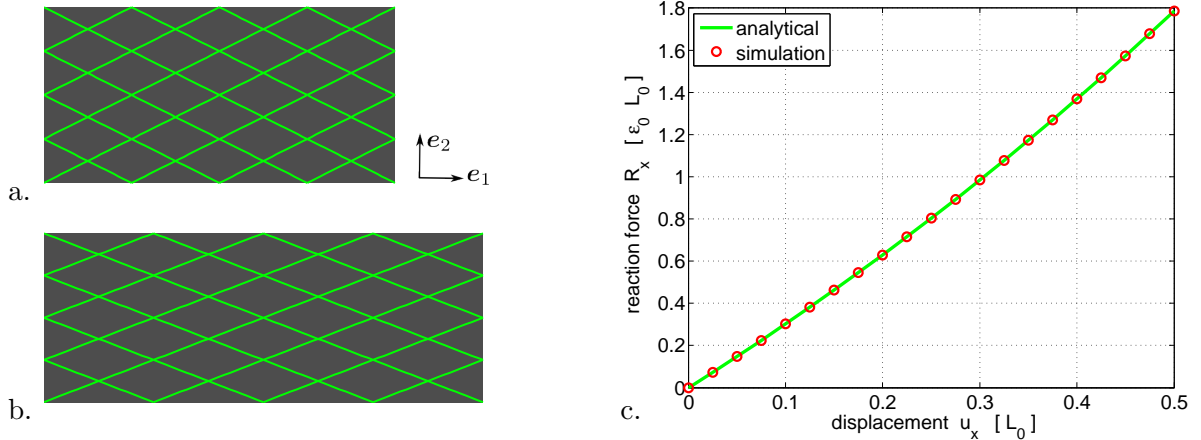


Figure 2: Uniaxial tension: (a.) Initial and (b.) deformed configurations with two fiber families (in green). (c.) Comparison with the analytical solution of Duong et al. [Duong et al. \(2021\)](#) for the reaction force R_x vs. displacement u_x at $X = 2 L_0$. Here, $\epsilon_L/2 = \mu = \epsilon_a = \epsilon_0$.

The first example considers uniaxial tension of a rectangular sheet of size $2L_0 \times L_0$ as shown in Fig. 2a-b. The sheet consists of two fiber families with initial directions $\mathbf{L}_1 = (2\mathbf{e}_1 + \mathbf{e}_2)/\sqrt{5}$ and $\mathbf{L}_2 = (2\mathbf{e}_1 - \mathbf{e}_2)/\sqrt{5}$. The top edge is free, while the left and bottom edges are fixed along \mathbf{e}_1 and \mathbf{e}_2 , respectively. The sheet is pulled by applying the displacement u_x on the right edge in the \mathbf{e}_1 direction. In this test we use the material parameters $\mu = \epsilon_a^{12} = \epsilon_0$, $\epsilon_L^i = 2\epsilon_0$, while $U(J)$ is set to zero, and β_n^i , β_g^i , and β_τ^i have no influence.

Fig. 2c shows the FE results in comparison to the exact solution. Our implementation is verified by obtaining an error within machine precision for a single finite element.

6.2 Pure shear

Next, our implementation is tested for pure shear. A square sheet with diagonal fibers is considered as shown in Fig. 3a. A Dirichlet boundary condition is applied on all edges, such that the sheet with initial dimension $L_0 \times L_0$ is deformed into the rectangular shape $\ell \times h$, with $\bar{\lambda} := \ell/L_0 = L_0/h$ (Fig. 3b). The material parameters are $\mu = \epsilon_0$, $\epsilon_L^i = 2\epsilon_0$, and $\epsilon_a^{12} = \epsilon_0$. Further, $U(J)$ is set to zero, while β_n^i , β_g^i , and β_τ^i have no influence.

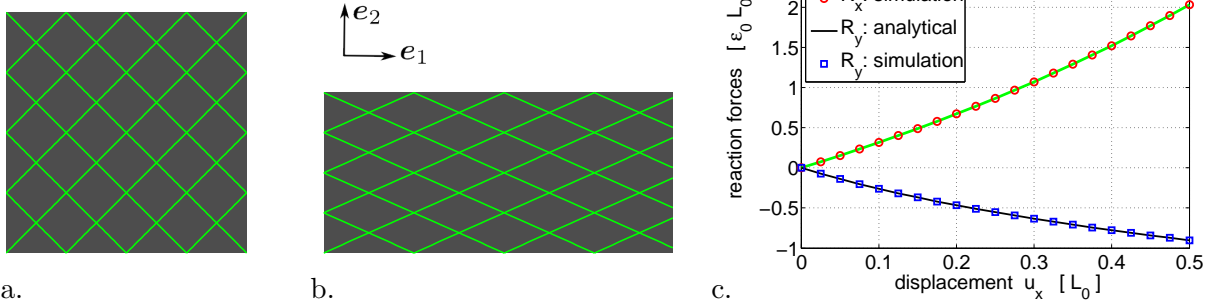


Figure 3: Pure shear: (a.) Initial and (b.) deformed configurations with two fiber families. (c.) Comparison with the exact solution (Duong et al., 2021) for the reaction forces vs. displacement u_x at $X = L_0$. Here, $\epsilon_L/2 = \epsilon_a = \mu = \epsilon_0$.

The exact solution for the reaction forces is (Duong et al., 2021)

$$\begin{aligned} R_x &= h \left[\mu (\bar{\lambda}^2 - 1) + \frac{1}{4} \epsilon_L (\bar{\lambda}^4 - 2\bar{\lambda}^2 + 1) + \frac{1}{4} \epsilon_a (\bar{\lambda}^4 - 1) \right], \\ R_y &= \ell \left[\mu \left(\frac{1}{\bar{\lambda}^2} - 1 \right) + \frac{1}{4\bar{\lambda}^4} \epsilon_L (\bar{\lambda}^4 - 2\bar{\lambda}^2 + 1) - \frac{1}{4\bar{\lambda}^4} \epsilon_a (\bar{\lambda}^4 - 1) \right]. \end{aligned} \quad (83)$$

Fig. 3c shows the comparison between the simulation and the exact solution. Again, we obtain an error within machine precision for a single finite element.

6.3 Picture frame test

The third example verifies our implementation in the picture frame test. A $L_0 \times L_0$ square sheet with two fiber families is considered as shown in Fig. 4a. The picture frame deformation (see Fig. 4b) is obtained by applying the Dirichlet boundary condition $\bar{\mathbf{x}}(\varphi, \bar{\mathbf{X}}) = \sqrt{2} (\cos \varphi \mathbf{e}_1 \otimes \mathbf{e}_1 + \sin \varphi \mathbf{e}_2 \otimes \mathbf{e}_2) \bar{\mathbf{X}}$ for every boundary node $\bar{\mathbf{X}}$ of the frame. The material parameters are taken as $\epsilon_a^{12} = \epsilon_0$, $U(J) = \mu = 0$, while ϵ_L^i , β_n^i , β_g^i , and β_τ^i have no influence. The exact solution of

the shear force (i.e. the tangential reaction) at an edge of the sheet is $R_s = -\epsilon_a^{12} \cos(2\varphi) L_0/2$, see e.g. Duong et al. (2021). Fig. 4c shows agreement between the simulation and the exact solution. Again, the error is within machine precision for a single finite element.

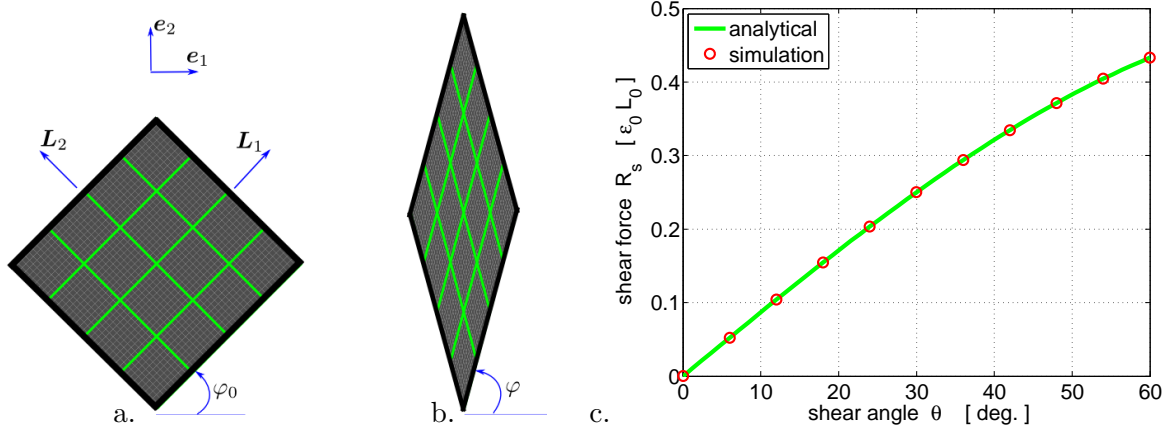


Figure 4: Picture frame test: (a.) Initial and (b.) deformed configurations with two fiber families. (c.) Comparison with the exact solution (Duong et al., 2021) for the shear force vs. shear angle $\theta := 2\varphi - 90^\circ$. Here, $\epsilon_a^{12} = \epsilon_0$.

6.4 Annulus expansion

The fourth example considers the homogeneous expansion of an annulus containing distributed circular fibers embedded in a matrix material. Due to the symmetry, only one fourth of the annulus is simulated as shown in Fig. 5a. Initially, the annulus has inner radius $R_i = L_0/2$ and outer radius $R_o = L_0$. A Dirichlet boundary condition is applied on the inner and outer boundary, such that they both expand with the stretch $\bar{\lambda} := r_i/R_i = r_o/R_o$, see Fig. 5b.

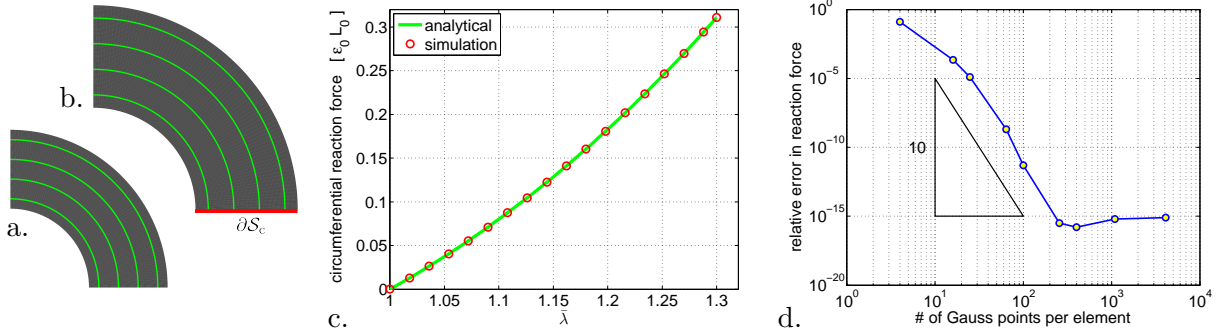


Figure 5: Annulus expansion: a. Initial and b. deformed configurations at $\bar{\lambda} = 1.3$ with distributed fibers. c. Circumferential reaction force vs. $\bar{\lambda}$ compared to the analytical solution (Duong et al., 2021). d. Relative error in the reaction force vs. the number of Gauss points. Here, the error is defined by $|R_{\text{num}} - R_{\text{exact}}|/R_{\text{exact}}$, where $R_{\text{num}} = \int_{\partial S_c} \boldsymbol{\nu} \boldsymbol{\sigma} \boldsymbol{\nu} ds$ and R_{exact} are the circumferential reaction forces according to the FE solution and the analytical solution, respectively, while $\boldsymbol{\nu}$ denotes the normal vector of the interface ∂S_c .

In order to induce a homogeneous deformation within the annulus, a graded matrix material with the surface dilatation energy $U(J) = \frac{1}{2} K (J - 1)^2$, where $K(R) = (\epsilon_L/2) \ln R$, is required in Eq. (68), see Duong et al. (2021). The material parameter $\epsilon_L = 2\epsilon_0$ is used, while β_n , β_τ , and β_g have no influence since K_n , T_g , and K_g are zero during deformation (Duong et al., 2021). Fig. 5c shows that the reaction force vs. stretch curve is in good agreement with the exact

solution. The error is within machine precision for a single finite element as long as numerical integration is sufficiently accurate as is shown in Fig. 5d.

6.5 Pure bending

The fifth example considers pure bending of a flat rectangular sheet of size $2.5 L_0 \times L_0$ subjected to the distributed moment M_{ext} (unit [moment/length]) along the two shorter edges as shown in Fig. 6a. The sheet contains a single fiber family in the \mathbf{e}_2 direction embedded in a matrix material. Here, the material parameters are taken as $\mu = 10 \epsilon_0$, $\beta_n = \epsilon_0 L_0^2$, and $\epsilon_L = 0$, while β_g and β_τ have no influence. The external moment deforms the sheet into a cylinder segment as seen in Fig. 6b.

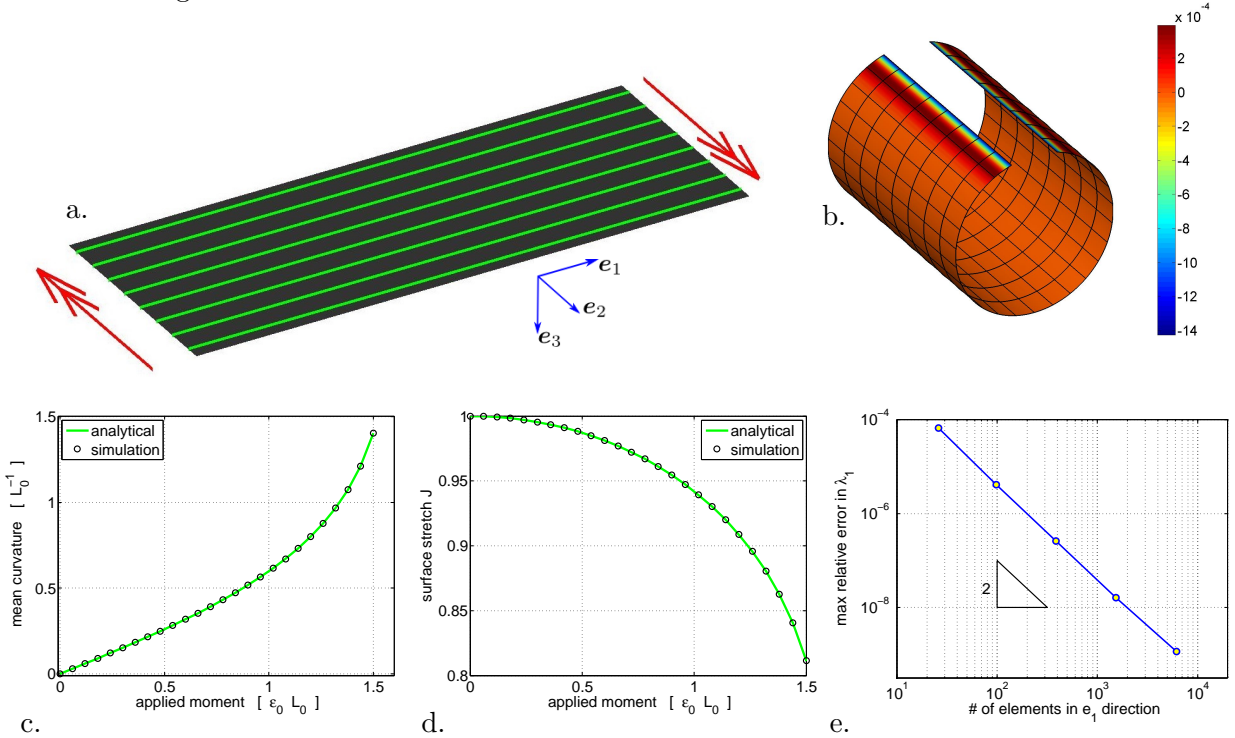


Figure 6: Pure bending of a flat sheet: a. Initial configuration ($2.5 L_0 \times L_0$) with fibers distributed along \mathbf{e}_1 . b. Deformed configuration colored by the relative error in the mean curvature. Comparisons with the exact solution are shown in (c.) for the mean curvature and in (d.) for surface stretch $J = \det_s \mathbf{F}$. e. Mesh convergence of the max relative error of $\bar{\lambda}_1$ (over the sample domain). Here, $\mu = 10 \epsilon_0$ and $\beta_n = \epsilon_0 L_0^2$.

According to Duong et al. [Duong et al. \(2021\)](#), the relationship

$$H = \frac{M_{\text{ext}}}{2 \beta_n \bar{\lambda}_1^4} \quad (84)$$

between the mean curvature H and external moment M_{ext} is obtained. Additionally, the exact solution for the stretch along the longer direction (due to high order effects) is

$$\bar{\lambda}_1 = \sqrt{\frac{1}{2} + \sqrt{\frac{1}{4} - \frac{1}{\mu \beta_n} M_{\text{ext}}^2}}, \quad \text{with} \quad M_{\text{ext}}^2 \leq \frac{1}{4} \mu \beta_n, \quad (85)$$

while the stretch along the shorter direction is $\bar{\lambda}_2 = 1$.

Figs. 6c-d demonstrate good agreement between the exact and FEM solution for the mean curvature H and surface stretch $J = \bar{\lambda}_1 \bar{\lambda}_2$. The convergence with mesh refinement plotted in Fig. 6e verifies the consistency of the finite element implementation.

7 Numerical examples: Inhomogenous deformation

This section demonstrates the performance of the proposed shell formulation by two tests: the bias extension and torsion tests of dry fabric sheets. Further, we fit material model (72)–(73) to the existing experimental data of Cao et al. Cao et al. (2008), and study the influence of in-plane bending.

7.1 Bias extension of woven fabrics

The first example studies the bias extension test for plain weave fabrics using material model (73) within the proposed shell formulation.

7.1.1 Bias extension of balanced weave fabrics: fitting to experimental data

We first fit material model (72)–(73) to the experimental data of Cao et al. Cao et al. (2008) for the bias extension test of balanced weave fabrics. In these fabrics, all fiber families are characterized by identical material properties. Two initially rectangular samples, #1 and #2, with dimension 115mm×230mm and 150mm×450mm, respectively, are used for the test. Two fiber families, initially aligned by $\pm 45^\circ$ w.r.t. the edges, are considered. The two samples are discretized by 16×32 and 16×48 quadratic NURBS elements, respectively. The samples are stretched in the longer direction by applying Dirichlet boundary conditions on the shorter edges.

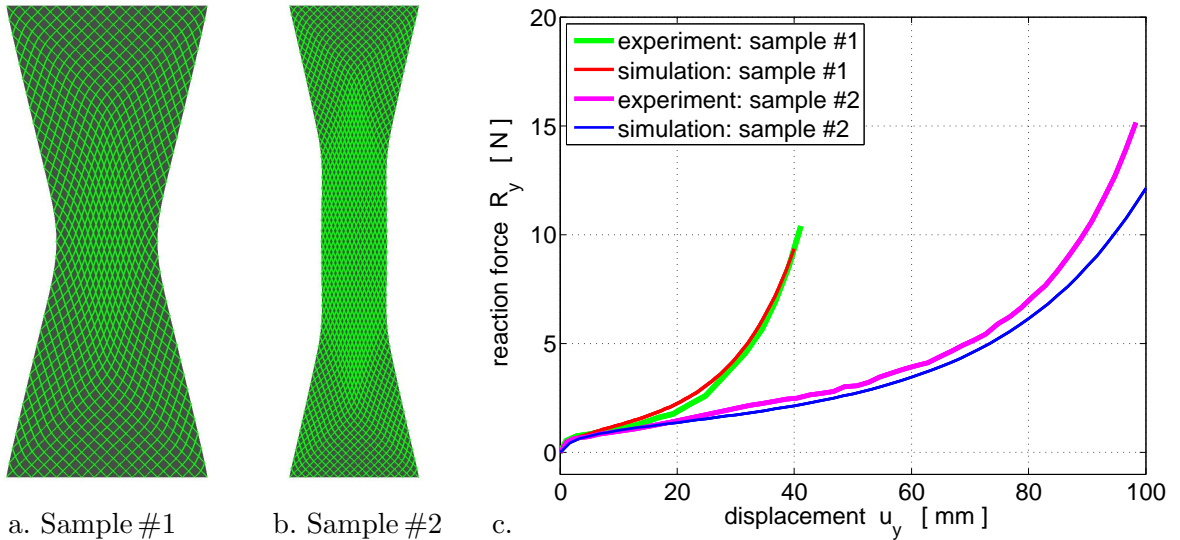


Figure 7: Bias extension test of plain weave fabrics: a-b. Deformed configurations of sample #1 and #2 at displacement 40mm and 100mm, respectively. The green lines show two fiber families. c. Reaction-displacement curves compared to the experimental data of Cao et al. Cao et al. (2008).

Figs. 7a-b show, that the two samples exhibit symmetric deformation in the bias extension test. Here, the material parameters of model (73) are obtained by fitting the load-displacement curve

of sample #1 to the experimental data of Cao et al. [Cao et al. \(2008\)](#). The fitted curve is plotted in Fig. 7c and the obtained parameters are listed in Tab. 1. The model is then validated by comparing the corresponding experimental results to the simulation for sample #2 as shown in Fig. 7c. As seen, the proposed model demonstrates good prediction at small and medium deformations but deviates from the experimental data at larger strains.

Remark 7.1: Note that the fit is based on a purely hyperelastic material model and hence does not capture plasticity. As plastic deformations usually play an important role in woven fabrics, in the form of fiber-fiber sliding, the presented model is only of limited use: It can help to understand the loading behavior, but it will not capture the unloading response correctly. For that a plasticity model should be included, which lies outside the scope of the present work.

7.1.2 Bias extension of balanced weave fabrics: the role of in-plane bending

Next, we investigate the influence of the in-plane bending stiffness β_g on the deformation, the load-displacement curve, and the finite element convergence behavior, using the bias extension test for sample #1. We use the material parameters from Tab. 1, but vary the in-plane bending stiffness β_g . In order to quantify the shear bands in the specimen, we examine the sum of the geodesic curvatures for the two fiber families, as $|\kappa_g^1| + |\kappa_g^2|$.

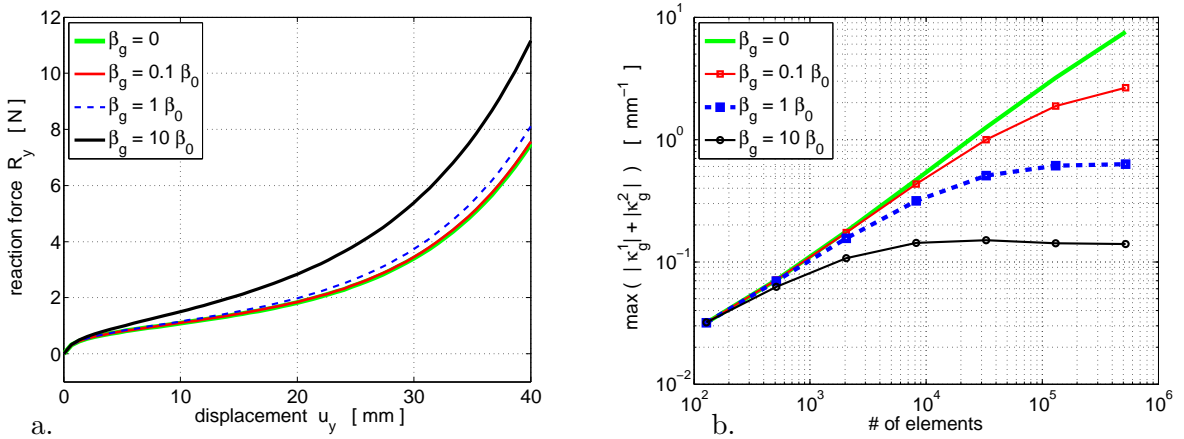


Figure 8: Bias extension of balanced weave fabric sample #1: a. Load-displacement curves for various in-plane bending stiffnesses β_g using 32×64 quadratic NURBS elements. b. Convergence of the shear bands measured by $\max(|\kappa_g^1| + |\kappa_g^2|)$ (over the sample domain) vs. mesh refinement. Here, $\beta_0 = 1.6 \text{ Nmm}$.

Fig. 8a shows the influence of β_g on the load-displacement curve. Accordingly, larger values of β_g lead to the significantly stiffer response. Fig. 8b shows the FE mesh convergence behavior of the shear bands measured by $\max(|\kappa_g^1| + |\kappa_g^2|)$. The quantity $|\kappa_g^1| + |\kappa_g^2|$ is also shown in Fig. 9 to visualize the shear bands for various in-plane bending stiffnesses. As expected, in case of zero in-plane bending stiffness ($\beta_g = 0$), the shear bands do not converge to a finite width.¹⁴ On the other hand, for $\beta_g > 0$, the shear bands converge to a finite width as observed in experiments (see e.g. [Boisse et al. \(2017\)](#)). The shear band width depends on the magnitude of the bending stiffness. Fig. 9 also shows that β_g visibly affects the width of the shear bands: they increase with β_g .

Fig. 10 shows the shear angle (first row), stress invariant $\text{tr}_s \boldsymbol{\sigma}$ (second row) and moment invariant $\text{tr}_s \bar{\boldsymbol{\mu}}_1$ (third row) for various values of β_g . Stress concentrations can be observed at the corners of the sample due to the high strains there.

¹⁴Without in-plane bending stiffness, the theoretical shear band width becomes zero, which is unphysical.

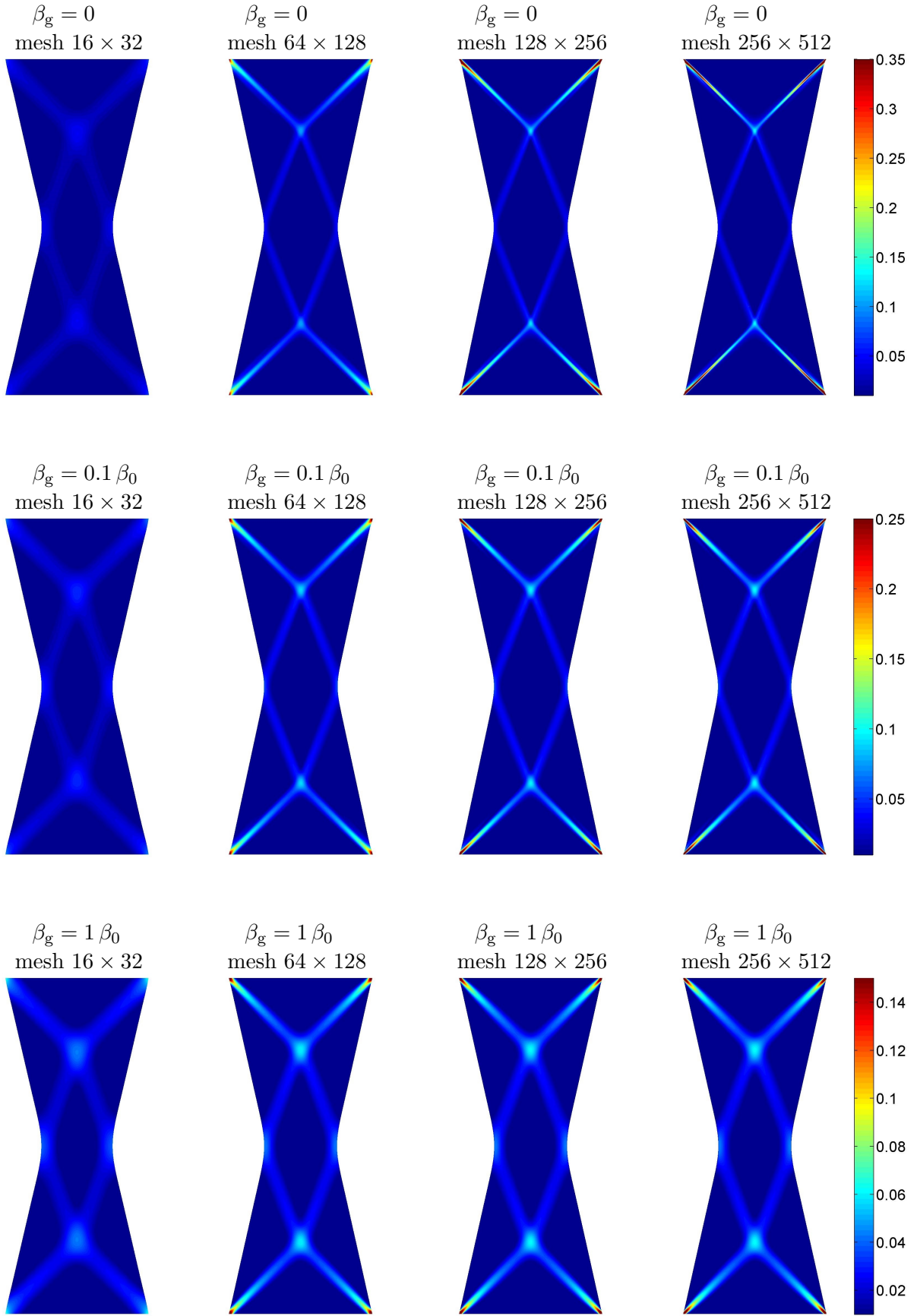


Figure 9: Bias extension of balanced weave fabric sample #1: $|\kappa_g^1| + |\kappa_g^2|$ (units $[\text{mm}^{-1}]$), a measure of shear bands, for various in-plane bending stiffnesses β_g (from top to bottom), and for various FE meshes (from left to right). The shear bands only converge for non-zero β_g . Here, $\beta_0 = 1.6\text{Nmm}$.

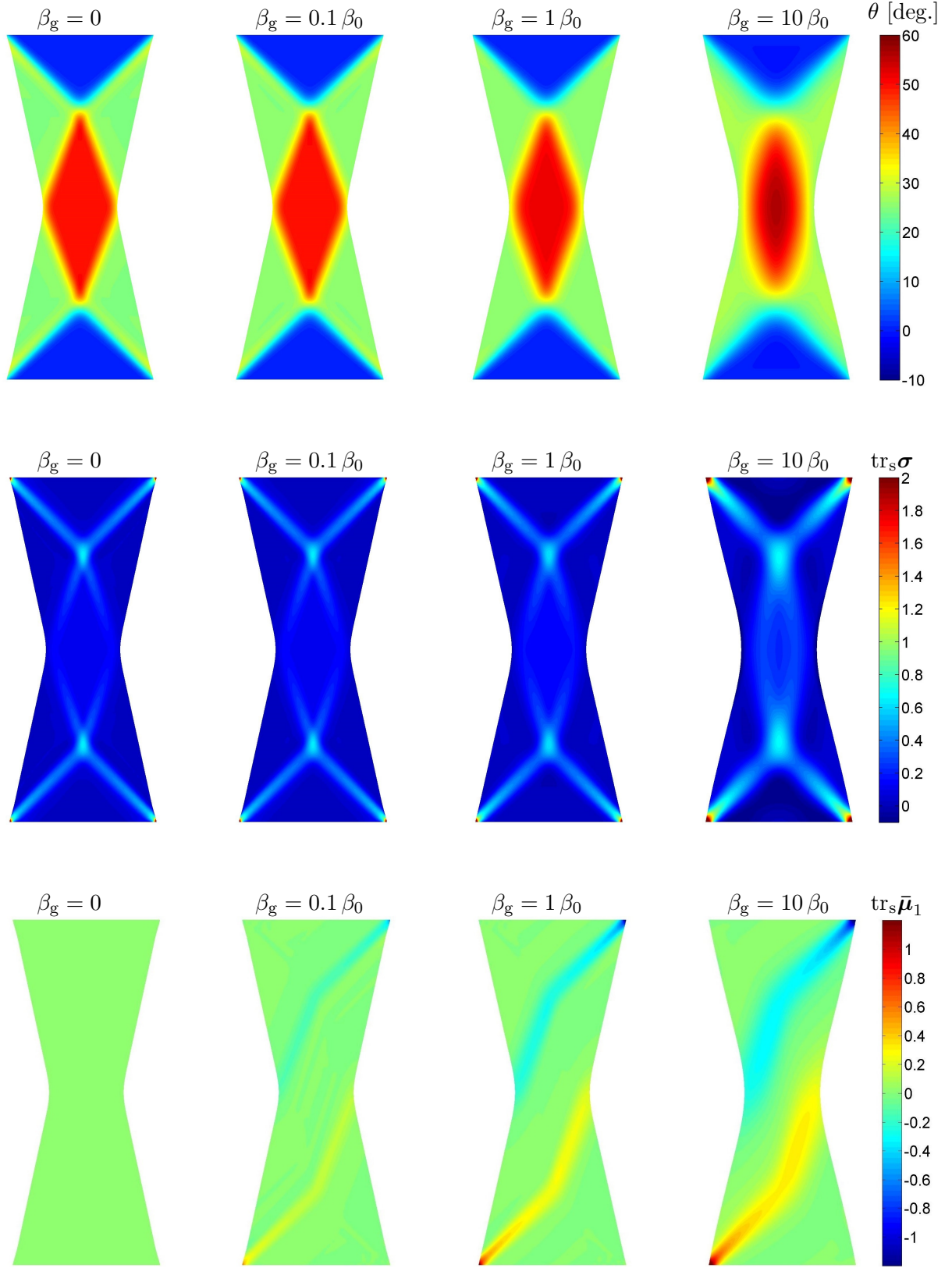


Figure 10: Bias extension of balanced weave fabric sample #1: shear angle $\theta := \arccos(\hat{\gamma}) - 90^\circ$ in degrees (first row), the first stress invariant $I_1 = \text{tr}_s \boldsymbol{\sigma}$ (second row, units [N/mm]), and the first moment invariant $\text{tr}_s \bar{\boldsymbol{\mu}}_1$ of fiber family #1 (third row, units [N]), all for various in-plane bending stiffnesses β_g , using $\beta_0 = 1.6 \text{ Nmm}$ and mesh 32×64 . The value of $\text{tr}_s \bar{\boldsymbol{\mu}}_1$ for $\beta_g = 0.1 \beta_0$ and $\beta_g = 1 \beta_0$ has been scaled by 20 and 5, respectively, w.r.t the actual value to increase visibility. (The distribution of $\text{tr}_s \bar{\boldsymbol{\mu}}_2$ of fiber family #2 (not shown) is the mirror image of $\text{tr}_s \bar{\boldsymbol{\mu}}_1$).

7.1.3 Bias extension of unbalanced weave fabrics: the role of in-plane bending

We further consider the influence of in-plane bending on the bias extension test for unbalanced weave fabrics – i.e. when the two fiber families have different material properties. This case can appear for example when the two families are made of different fiber materials, see e.g. [Madeo et al. \(2016\)](#). We assume here that only the in-plane bending stiffness is different, while all other parameters are equal. Sample #2 and constitutive model (72)–(73) with the parameters from Tab. 1 are used again but now both β_g^1 and β_g^2 are varied. The difference in bending stiffness of the fiber families is characterized by the ratio $r_b := \beta_g^2/\beta_g^1$.

Fig. 11 shows the deformed shapes of the sample for various bending stiffnesses β_g^1 and β_g^2 . As expected, unsymmetric sample shapes are obtained for $r_b > 1$, especially when β_g^2 is large. This is in qualitative agreement with the experimental results given by [Madeo et al. \(2016\)](#).

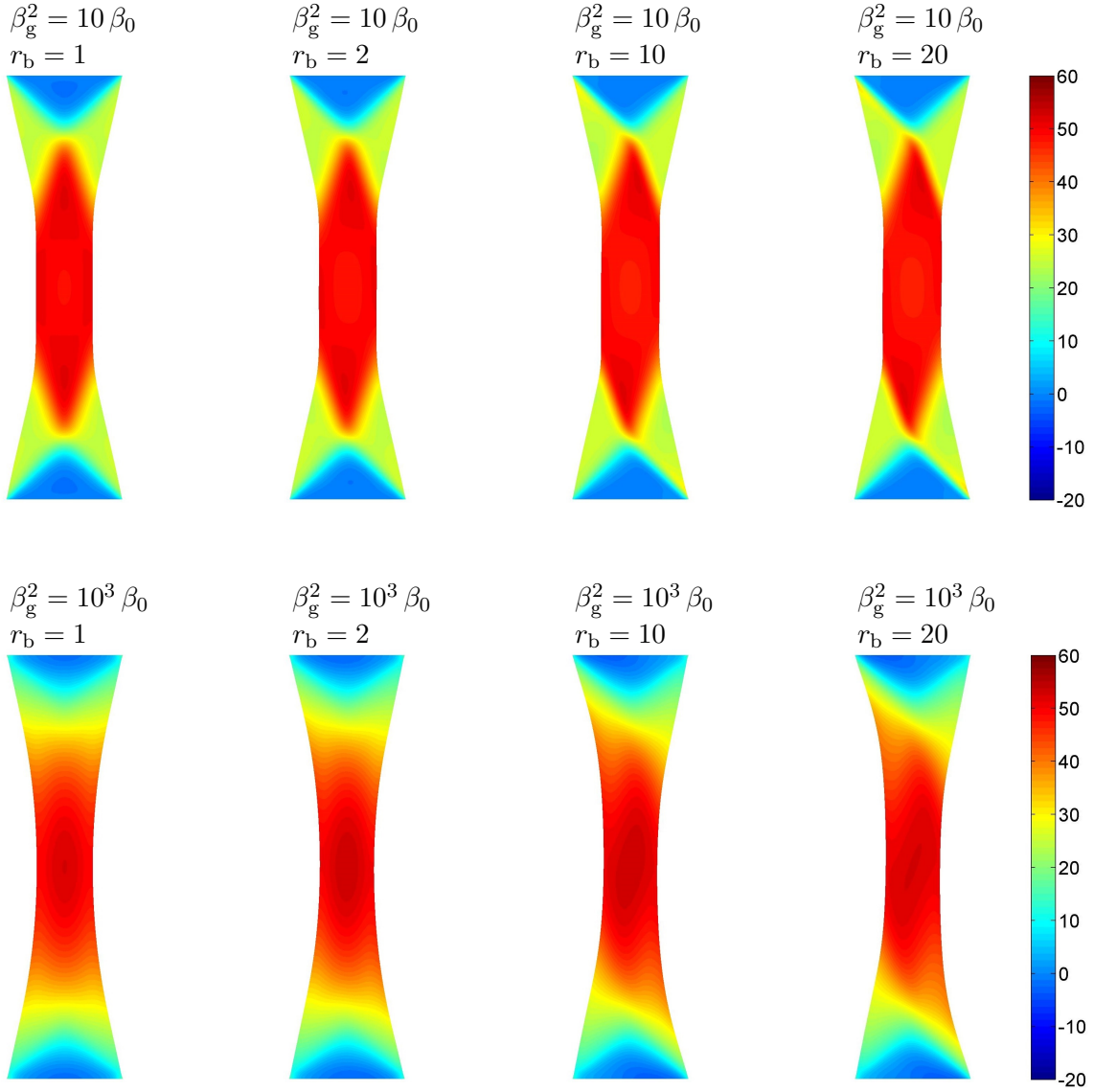


Figure 11: Bias extension of unbalanced weave fabric sample #2: Deformed configuration for various $r_b = \beta_g^2/\beta_g^1$ (from left to right) and various in-plane bending stiffnesses β_g^2 (from top to bottom). The color shows the shear angle $\theta := \arccos(\hat{\gamma}) - 90^\circ$ in degrees. Here, $\beta_0 = 1.6\text{Nmm}$.

7.2 Torsion of dry fabrics

The second example considers the torsion of a rectangular sheet with dimension $2L_0 \times L_0$ as shown in Fig. 12a. The left edge is fixed in all three directions, while the right edge is only fixed along \mathbf{e}_1 . The two longer edges are free. A twisting angle $\bar{\phi}$ is applied around the center line on the right edge from 0° to 180° with 1° per load step. The sheet contains dry fabrics with two fiber families, initially aligned by $\pm 45^\circ$ w.r.t. the \mathbf{e}_1 direction. Material model (67)–(68) is used. The sheet is discretized by 50×25 quadratic NURBS elements. In order to capture wrinkling of the sheet (if any), a random imperfection of X_3 is imposed (following a standard distribution) as shown in Fig. 12b. Further, to deal with possible out-of-plane instability due to wrinkling, a small viscosity ($\epsilon = \epsilon_0$) is added for stabilization (see e.g. Duong (2017)).

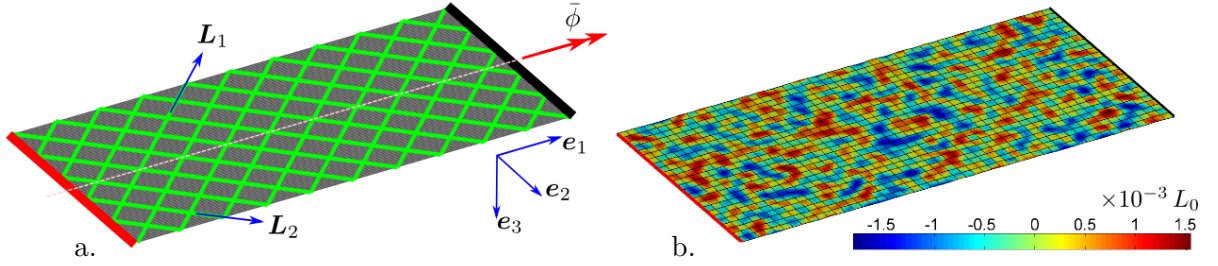


Figure 12: Torsion of dry fabrics : a. Fabric specimen, boundary conditions, and fiber directions L_1 and L_2 of two fiber families. A rotation is applied around the center axis (dashed line) on the right edge. b. Corresponding FE mesh with a small imperfection in the X_3 -coordinate obtained by randomly displacing the control points in the \mathbf{e}_3 direction following a normal distribution with standard deviation $1.1 \times 10^{-3} L_0$.

7.2.1 Nearly incompressible fibers

We first consider the case with axially nearly inextensible and incompressible fibers. Therefore, the material parameters are taken as $\epsilon_L = 4 \epsilon_{\text{stab}}^e = 2000 \epsilon_0$, $\epsilon_a = \epsilon_0$, and $\beta_n = \beta_g = \beta_\tau = \epsilon_0 L_0^2$, while μ and ϵ_{stab}^v are zero.

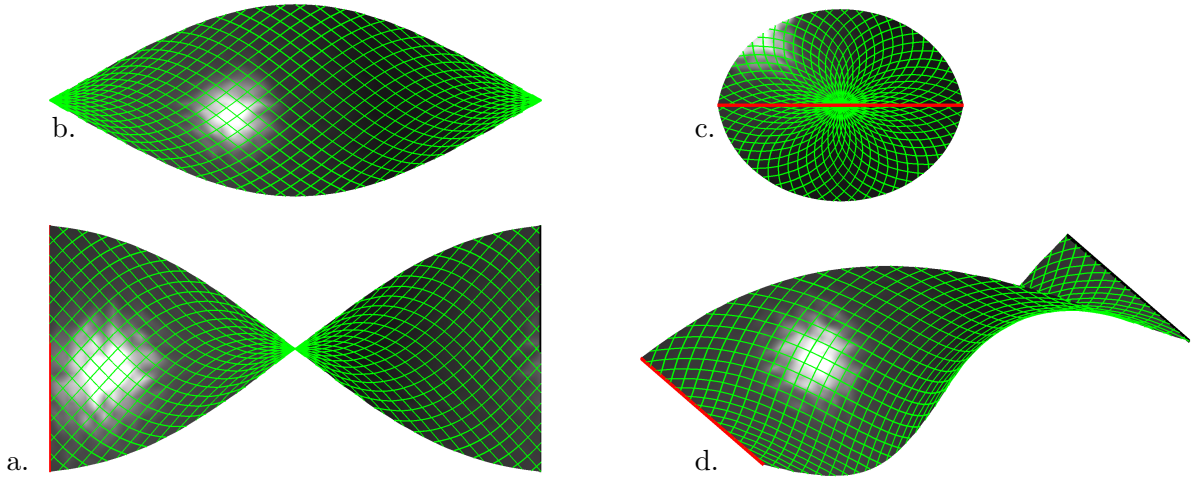


Figure 13: Torsion of dry fabrics with nearly incompressible fibers: Deformed configuration at $\bar{\phi} = 180^\circ$ showing embedded fibers in a. top view, b. front view, c. side view, and d. 3D view.

Fig. 13 shows the deformed configuration with the embedded fibers at $\bar{\phi} = 180^\circ$. As seen, the deformed sheet behaves similar to an isotropic elastic shell, and no wrinkling occurs in spite of the geometrical imperfection in the out-of-plane direction.¹⁵

Fig. 14a plots the reaction-twisting curve, which shows that both the reaction force and the reaction moment are monotonically increasing. As seen in Fig. 14b, most of the strain energy initially goes into out-of-plane bending. However, as the twisting angle increases, the in-plane fiber bending energy increases significantly, while the other membrane energies remain relatively small.

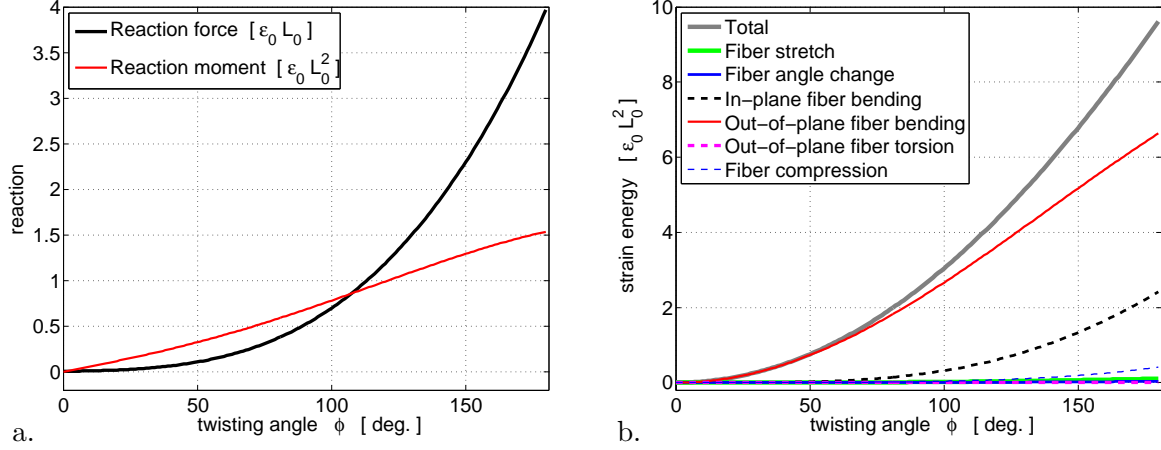


Figure 14: Torsion of dry fabrics with nearly incompressible fibers: a. Support reactions and b. strain energies (integrated strain energy densities) of the sheet versus twisting angle $\bar{\phi}$.

7.2.2 Effectively compressible fibers

Next, we consider fabrics with effectively compressible fibers based on the phenomenological model of Sec. 5 that accounts for the microscale buckling of compressed fibers. To this end, we reset material parameter $\epsilon_{\text{stab}}^e = 5 \epsilon_0$ and $\epsilon_{\text{stab}}^v = 250 \epsilon_0$, while the other parameters remain unchanged.

Fig. 15 shows the deformed configuration with embedded fibers at $\bar{\phi} = 180^\circ$. As seen, the center of the sheet is compressed significantly in the lateral direction, and consequently macroscopic wrinkling can be seen there as shown in Fig. 15e. As Fig. 16 shows, fibers (of either family) are compressed not only at the sheet center, but also along the diagonals of the sheet. This implies that microscopic fiber buckling can also occur along the diagonals.

Figs. 17a-b plot the reaction-twisting curves and the strain energies of the sheet, respectively. Similar to the incompressible case, most of the strain energy initially goes into out-of-plane bending, but the out-of-plane energy loses convexity and is exceeded by the in-plane bending energy as the twisting angle increases. This implies that the fibers become unstable in out-of-plane bending. The resulting deformation and the reaction-twisting curve are shown in Fig. 16 and Fig. 17a, respectively.

¹⁵A similar deformed shape is also obtained in the simulation result of Schulte et al. [Schulte et al. \(2020\)](#).

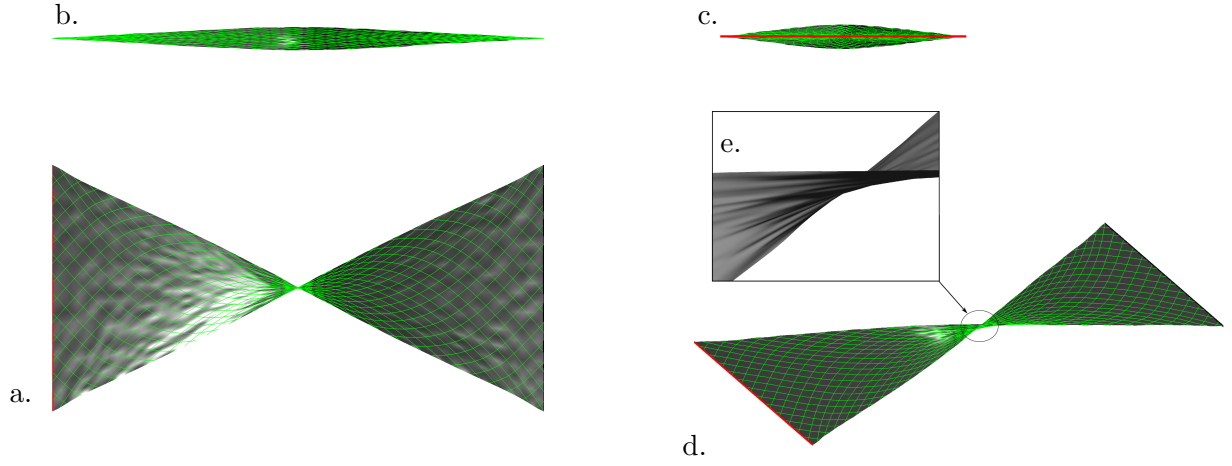


Figure 15: Torsion of dry fabrics with effectively compressible fibers: Deformed configuration at $\bar{\phi} = 180^\circ$ showing embedded fibers in a. top view, b. front view, c. side view, d. 3D view, and e. zoom into the sheet center.

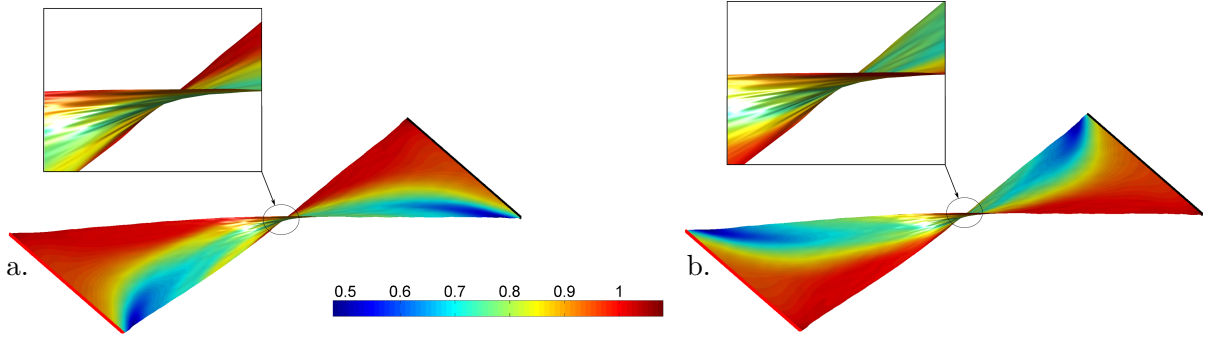


Figure 16: The torsion test for dry fabrics of compressible fibers: Deformed configuration at $\bar{\phi} = 180^\circ$ showing invariant Λ^1 (a.) and Λ^2 (b.).

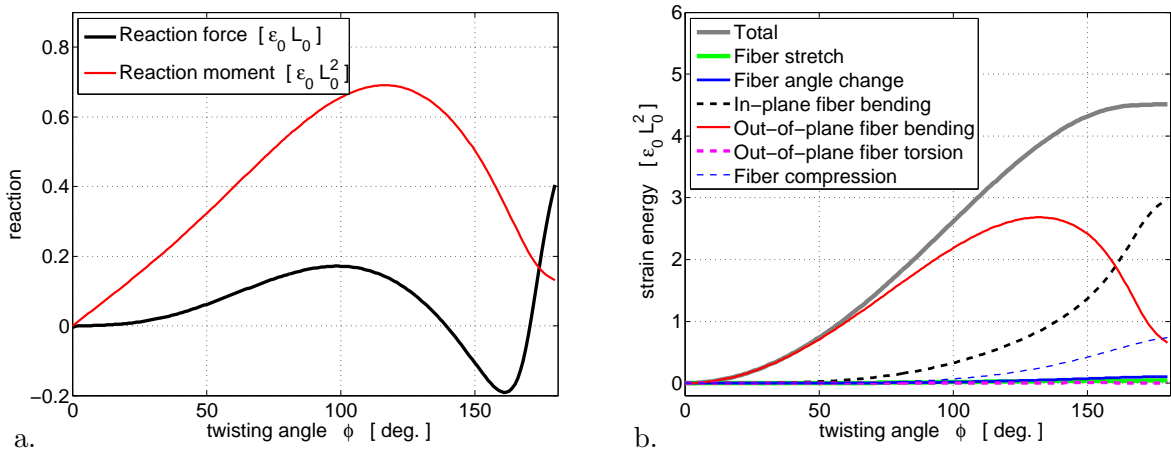


Figure 17: The torsion test for dry fabrics of effectively compressible fibers: a. Reactions and b. strain energies (integrated strain energy densities) of the sheet versus twisting angle $\bar{\phi}$.

8 Conclusion

We have presented a nonlinear rotation-free isogeometric shell formulation that can capture the in-plane bending behavior of embedded fibers. The formulation is based on the generalized Kirchhoff-Love shell theory of Duong et al. [Duong et al. \(2021\)](#). Its finite element implementation can be directly obtained from the isogeometric FE formulation of Duong et al. [Duong et al. \(2017\)](#) by complementing it with the additional in-plane bending term. The construction of material models for the proposed shell formulation can follow that of classical shells, since inducing invariants for the relative in-plane curvature tensor $\bar{\mathbf{K}}$ is very similar to that of the relative out-of-plane curvature tensor \mathbf{K} . We have demonstrated this point by proposing two material models for fabrics in Sec. 5. The woven fabric model of Sec. 5.2 shows good agreement with existing experiment data for the bias extension test. With this material model, the influence of the in-plane bending stiffness on the bias extension test has been investigated for both balanced and unbalanced weave fabrics. The proposed shell formulation can also admit a wide range of other material models including those expressed directly in surface energy form and those obtained from thickness integration of 3D material models. In order to suppress possible material instabilities due to fiber compression, we have added a stabilization term within the proposed shell formulation. Finally, the accuracy and robustness of the proposed formulation is verified by several numerical examples, characterized by both homogenous and inhomogenous deformation in Sec. 6 and 7, respectively. Our formulation can be extended to capture inter-ply and intra-ply sliding of yarns, which will be a subject of future work.

A Tangent matrices of the external forces

This appendix summarizes the linearization and discretization of the external virtual work term (40) appearing in the weak form.

A.1 Linearization of the external virtual work

For the first term of G_{ext} in Eq. (40), no linearization is required as $\mathbf{f}_0 dA$ is constant for dead loading. The linearization of the remaining terms in Eq. (40) can be found as (see also [Sauer et al. \(2014\)](#); [Sauer and Duong \(2017\)](#); [Duong et al. \(2017\)](#))

$$\begin{aligned}
\Delta G_{\text{ext}} = & \int_{\mathcal{S}} \delta \mathbf{x} p (\mathbf{n} \otimes \mathbf{a}^\alpha - \mathbf{a}^\alpha \otimes \mathbf{n}) \Delta \mathbf{a}_\alpha d\mathbf{a} \\
& + \int_{\partial_t \mathcal{S}} \delta \mathbf{x} \mathbf{t} \otimes \mathbf{a}_\xi \frac{1}{\|\mathbf{a}_\xi\|^2} \Delta \mathbf{a}_\xi d\mathbf{s} - \delta \mathbf{x} m_\nu (\mathbf{a}^\alpha \otimes \mathbf{n}) \Delta \mathbf{a}_\alpha \\
& + \int_{\partial_m \mathcal{S}} \delta \mathbf{a}_\alpha (\nu^\alpha \mathbf{a}^\beta \otimes \mathbf{n} + \nu^\beta \mathbf{n} \otimes \mathbf{a}^\alpha) \Delta \mathbf{a}_\beta m_\tau d\mathbf{s} \\
& - \int_{\partial_m \mathcal{S}} \delta \mathbf{a}_\alpha \nu^\alpha \mathbf{n} \otimes \mathbf{a}_\xi \frac{1}{\|\mathbf{a}_\xi\|^2} \Delta \mathbf{a}_\xi m_\tau d\mathbf{s} + \int_{\partial_m \mathcal{S}} \delta \mathbf{a}_\alpha \tau^\alpha \mathbf{n} \otimes \nu \frac{1}{\|\mathbf{a}_\xi\|} \Delta \mathbf{a}_\xi m_\tau d\mathbf{s} \\
& + \int_{\partial_{\bar{m}} \mathcal{S}} \delta \mathbf{a}_\alpha [\ell^\alpha c^\beta \mathbf{n} \otimes \mathbf{n} - \ell^{\alpha\beta} (\boldsymbol{\ell} \otimes \mathbf{c} + \mathbf{c} \otimes \boldsymbol{\ell})] \Delta \mathbf{a}_\beta \bar{m} d\mathbf{s} \\
& + \int_{\partial_{\bar{m}} \mathcal{S}} \delta \mathbf{a}_\alpha \ell^\alpha \mathbf{c} \otimes \mathbf{a}_\xi \Delta \mathbf{a}_\xi \frac{\bar{m}}{\|\mathbf{a}_\xi\|^2} d\mathbf{s} ,
\end{aligned} \tag{86}$$

where p is assumed to be constant, and ξ is the convective coordinate along the boundary, so that $\boldsymbol{\tau} = \mathbf{a}_\xi / \|\mathbf{a}_\xi\|$ and $\Delta \mathbf{d}s = (\mathbf{a}_\xi / \|\mathbf{a}_\xi\|) \cdot \Delta \mathbf{a}_\xi \, ds$. For the last term in Eq. (86), we have used Eq. (38) and $\Delta \ell^\alpha = -\ell^{\alpha\beta} \boldsymbol{\ell} \cdot \Delta \mathbf{a}_\beta$ (see Duong et al. (2021)).

A.2 Discretization of the external virtual work

The tangent matrices in Eq. (66) follow from applying discretization to Eq. (86), which gives

$$\begin{aligned}
\mathbf{k}_{\text{ext}p}^e &= \int_S \mathbf{N}^T p (\mathbf{n} \otimes \mathbf{a}^\alpha - \mathbf{a}^\alpha \otimes \mathbf{n}) \mathbf{N}_{,\alpha} \, da , \\
\mathbf{k}_{\text{ext}t}^e &= \int_{\partial_t S} \mathbf{N}^T \mathbf{t} \otimes \mathbf{a}_\xi \frac{1}{\|\mathbf{a}_\xi\|^2} \mathbf{N}_{,\xi} \, ds , \\
\mathbf{k}_{\text{ext}\nu}^n &= -m_\nu (\mathbf{a}^\alpha \otimes \mathbf{n}) \mathbf{N}_{,\alpha} , \\
\mathbf{k}_{\text{ext}m}^e &= \int_{\partial_m S} \mathbf{N}_{,\alpha}^T (\nu^\alpha \mathbf{a}^\beta \otimes \mathbf{n} + \nu^\beta \mathbf{n} \otimes \mathbf{a}^\alpha) \mathbf{N}_{,\beta} m_\tau \, ds \\
&\quad + \int_{\partial_m S} \mathbf{N}_{,\alpha}^T \nu^\alpha \mathbf{n} \otimes \mathbf{a}_\xi \mathbf{N}_{,\xi} \frac{m_\tau}{\|\mathbf{a}_\xi\|^2} \, ds + \left[\int_{\partial_m S} \mathbf{N}_{,\alpha}^T \tau^\alpha \mathbf{n} \otimes \boldsymbol{\nu} \mathbf{N}_{,\xi} \frac{m_\tau}{\|\mathbf{a}_\xi\|} \, ds \right] , \\
\mathbf{k}_{\text{ext}\bar{m}}^e &= \int_{\partial_{\bar{m}} S} \mathbf{N}_{,\alpha}^T [\ell^\alpha c^\beta \mathbf{n} \otimes \mathbf{n} - \ell^{\alpha\beta} (\boldsymbol{\ell} \otimes \mathbf{c} + \mathbf{c} \otimes \boldsymbol{\ell})] \mathbf{N}_{,\beta} \bar{m} \, ds \\
&\quad + \int_{\partial_{\bar{m}} S} \mathbf{N}_{,\alpha}^T \ell^\alpha \mathbf{c} \otimes \mathbf{a}_\xi \mathbf{N}_{,\xi} \frac{\bar{m}}{\|\mathbf{a}_\xi\|^2} \, ds .
\end{aligned} \tag{87}$$

Remark A.1: The tangent matrices in Eq. (87) account for live loading. In case $\mathbf{t} \, ds$, $m_\tau \, ds$, and $\bar{m} \, ds$ are constant, the last term in $\mathbf{k}_{\text{ext}t}^e$, the last two terms in $\mathbf{k}_{\text{ext}m}^e$, and the last term in $\mathbf{k}_{\text{ext}\bar{m}}^e$ vanish, respectively.

Remark A.2: Note, that the last term in $\mathbf{k}_{\text{ext}m}^e$ (in square bracket) accounts for the variation of $\boldsymbol{\nu}$, which is missing in Duong et al. (2017) (cf. Appendix A, Eq. (128)).

B Efficient FE implementation

This appendix presents an efficient implementation of Eq. (54) for the Newton-Raphson method. The implementation can be viewed as an extension of Duong et al. (2017) by the in-plane bending term.

Since Eq. (54) holds for all nodal variations $\delta \mathbf{x}$, it leads, after the application of the essential boundary conditions, to the system of nonlinear equations

$$\mathbf{f}(\mathbf{u}) := \mathbf{f}_{\text{int}} + \mathbf{f}_{\text{ext}} = \mathbf{0} , \tag{88}$$

where \mathbf{u} are the nodal unknowns, and \mathbf{f}_{int} and \mathbf{f}_{ext} are the global FE forces obtained from assembling the elemental FE forces given by Eqs. (56) and (58), respectively.

During Newton-Raphson, Eq. (88) is solved iteratively for the increment $\Delta \mathbf{u}$ from

$$\begin{aligned}
\mathbf{K}(\mathbf{u}^{i-1}) \Delta \mathbf{u}^i &= -\mathbf{f}(\mathbf{u}^{i-1}) , \\
\mathbf{u}^i &= \mathbf{u}^{i-1} + \Delta \mathbf{u}^i ,
\end{aligned} \tag{89}$$

where \mathbf{K} is the (reduced) global stiffness matrix. It is obtained by assembling the elemental tangent matrices, i.e.

$$\mathbf{K} = \sum_{e=1}^{n_{\text{el}}} (\mathbf{k}_{\text{mat}}^e + \mathbf{k}_{\text{geo}}^e + \mathbf{k}_{\text{ext}}^e) , \quad (90)$$

and then eliminating the constrained degrees of freedom. Here, $\mathbf{k}_{\text{mat}}^e$, $\mathbf{k}_{\text{geo}}^e$, and $\mathbf{k}_{\text{ext}}^e$ are defined by Eqs. (60), (62), and (66), respectively.

B.1 Implementation of FE force vectors

Due to the symmetry of the stress and moment tensors, they can be represented compactly in Voigt notation as

$$\hat{\boldsymbol{\tau}} := [\tau^{11} , \tau^{22} , \tau^{12}]^T , \quad \hat{\mathbf{M}}_0 := [M_0^{11} , M_0^{22} , M_0^{12}]^T , \quad \hat{\bar{\mathbf{M}}}_0 := [\bar{M}_0^{11} , \bar{M}_0^{22} , \bar{M}_0^{12}]^T . \quad (91)$$

Defining the $3n_{\text{ne}} \times 1$ arrays

$$\begin{aligned} \mathbf{L}_{\alpha\beta}^a &:= \mathbf{N}_{,\alpha}^T \mathbf{a}_{\beta} , \\ \mathbf{L}_{\alpha}^n &:= \mathbf{N}_{,\alpha}^T \mathbf{n} , \\ \mathbf{G}_{\alpha\beta}^n &:= \mathbf{N}_{;\alpha\beta}^T \mathbf{n} \\ \mathbf{G}_{\alpha\beta}^a &:= -\mathbf{N}_{,\alpha}^T \bar{\mathbf{c}}_{,\beta} - \mathbf{C}_{,\beta}^T \mathbf{a}_{\alpha} , \end{aligned} \quad (92)$$

where n_{ne} is the number of control points per element, and organizing them into the arrays

$$\begin{aligned} \hat{\mathbf{L}}_a &:= [\mathbf{L}_{11}^a , \mathbf{L}_{22}^a , \mathbf{L}_{12}^a + \mathbf{L}_{21}^a] , \\ \hat{\mathbf{G}}_n &:= [\mathbf{G}_{11}^n , \mathbf{G}_{22}^n , \mathbf{G}_{12}^n + \mathbf{G}_{21}^n] , \\ \hat{\mathbf{G}}_a &:= [\mathbf{G}_{11}^a , \mathbf{G}_{22}^a , \mathbf{G}_{12}^a + \mathbf{G}_{21}^a] , \end{aligned} \quad (93)$$

the FE forces (56) can be implemented as

$$\mathbf{f}_{\text{int}\tau}^e = \int_{\Omega_0^e} \hat{\mathbf{L}}_a \hat{\boldsymbol{\tau}} \, dA , \quad \mathbf{f}_{\text{int}M}^e = \int_{\Omega_0^e} \hat{\mathbf{G}}_n \hat{\mathbf{M}}_0 \, dA , \quad \mathbf{f}_{\text{int}\bar{M}}^e = \int_{\Omega_0^e} \hat{\mathbf{G}}_a \hat{\bar{\mathbf{M}}}_0 \, dA . \quad (94)$$

Note, that for classical shell formulations without fiber bending, the last term and its associated tangent matrices are simply dropped.

B.2 Implementation of material stiffness matrices

To implement the material stiffness matrices, the nine material tangents $c^{\alpha\beta\gamma\delta}$, $d^{\alpha\beta\gamma\delta}$, $e^{\alpha\beta\gamma\delta}$, $f^{\alpha\beta\gamma\delta}$, $\bar{d}^{\alpha\beta\gamma\delta}$, $\bar{e}^{\alpha\beta\gamma\delta}$, $\bar{f}^{\alpha\beta\gamma\delta}$, $\bar{g}^{\alpha\beta\gamma\delta}$, and $\bar{h}^{\alpha\beta\gamma\delta}$ are arranged into the 3×3 matrices \mathbf{C} , \mathbf{D} , \mathbf{E} , \mathbf{F} , $\bar{\mathbf{D}}$, $\bar{\mathbf{E}}$, $\bar{\mathbf{F}}$, $\bar{\mathbf{G}}$, $\bar{\mathbf{H}}$, respectively, as, for instance,

$$\mathbf{C} := \begin{bmatrix} c^{1111} & c^{1122} & c^{1112} \\ c^{2211} & c^{2222} & c^{2212} \\ c^{1211} & c^{1222} & c^{1212} \end{bmatrix} . \quad (95)$$

Note, that for hyperelastic material models, we further have $\mathbf{C} = \mathbf{C}^T$, $\mathbf{E} = \mathbf{D}^T$, $\mathbf{F} = \mathbf{F}^T$, $\bar{\mathbf{E}} = \bar{\mathbf{D}}^T$, $\bar{\mathbf{F}} = \bar{\mathbf{F}}^T$, $\bar{\mathbf{G}} = \bar{\mathbf{H}}^T$. With these and Eq. (93), the material stiffness matrices in

Eq. (61) can be implemented as

$$\begin{aligned}
\mathbf{k}_{\tau\tau}^e &= \int_{\Omega_0^e} \hat{\mathbf{L}}_a \mathbf{C} \hat{\mathbf{L}}_a^T dA, & \mathbf{k}_{\tau M}^e &= \int_{\Omega_0^e} \hat{\mathbf{L}}_a \bar{\mathbf{D}} \hat{\mathbf{G}}_a^T dA, \\
\mathbf{k}_{\tau M}^e &= \int_{\Omega_0^e} \hat{\mathbf{L}}_a \mathbf{D} \hat{\mathbf{G}}_n^T dA, & \mathbf{k}_{MM}^e &= \int_{\Omega_0^e} \hat{\mathbf{G}}_n \bar{\mathbf{E}} \hat{\mathbf{G}}_n^T dA, \\
\mathbf{k}_{M\tau}^e &= \int_{\Omega_0^e} \hat{\mathbf{G}}_n \mathbf{E} \hat{\mathbf{L}}_a^T dA, & \mathbf{k}_{M\tau}^e &= \int_{\Omega_0^e} \hat{\mathbf{G}}_a \bar{\mathbf{F}} \hat{\mathbf{L}}_a^T dA, \\
\mathbf{k}_{MM}^e &= \int_{\Omega_0^e} \hat{\mathbf{G}}_n \mathbf{F} \hat{\mathbf{G}}_n^T dA, & \mathbf{k}_{MM}^e &= \int_{\Omega_0^e} \hat{\mathbf{G}}_a \bar{\mathbf{G}} \hat{\mathbf{G}}_n^T dA, \\
& & \mathbf{k}_{MM}^e &= \int_{\Omega_0^e} \hat{\mathbf{G}}_a \bar{\mathbf{H}} \hat{\mathbf{G}}_a^T dA.
\end{aligned} \tag{96}$$

Compared to classical Kirchhoff-Love shell theory, the five terms on the right hand side are additional terms due to in-plane bending.

B.3 Implementation of geometrical matrices

Using (92) and (93), the geometric stiffness matrices in Eq. (63) can be implemented as

$$\begin{aligned}
\mathbf{k}_\tau^e &= - \int_{\Omega_0^e} \left(\tau^{11} \mathbf{N}_{,1}^T \mathbf{N}_{,1} + \tau^{22} \mathbf{N}_{,2}^T \mathbf{N}_{,2} + \tau^{12} \mathbf{N}_{,1}^T \mathbf{N}_{,2} + \tau^{21} \mathbf{N}_{,2}^T \mathbf{N}_{,1} \right) dA, \\
\mathbf{k}_M^e &= - \int_{\Omega_0^e} b_M \left[a^{11} \mathbf{L}_1^n \mathbf{L}_1^{nT} + a^{22} \mathbf{L}_2^n \mathbf{L}_2^{nT} + a^{12} (\mathbf{L}_1^n \mathbf{L}_2^{nT} + \mathbf{L}_2^n \mathbf{L}_1^{nT}) \right] dA \\
&\quad - \int_{\Omega_0^e} \left(\mathbf{L}_1^n (\mathbf{a}^1)^T + \mathbf{L}_2^n (\mathbf{a}^2)^T \right) \left(M_0^{11} \mathbf{N}_{;11} + M_0^{22} \mathbf{N}_{;22} + 2 M_0^{12} \mathbf{N}_{;12} \right) dA, \\
\mathbf{k}_M^e &= - \int_{\Omega_0^e} \left(\bar{M}_0^{11} \mathbf{N}_{,1}^T \mathbf{C}_{,1} + \bar{M}_0^{22} \mathbf{N}_{,2}^T \mathbf{C}_{,2} + \bar{M}_0^{12} \mathbf{N}_{,1}^T \mathbf{C}_{,2} + \bar{M}_0^{21} \mathbf{N}_{,2}^T \mathbf{C}_{,1} \right) dA \\
&\quad - \int_{\Omega_0^e} \left(\bar{M}_0^{11} \mathbf{C}_{,1}^T \mathbf{N}_{,1} + \bar{M}_0^{22} \mathbf{C}_{,2}^T \mathbf{N}_{,2} + \bar{M}_0^{12} \mathbf{C}_{,2}^T \mathbf{N}_{,1} + \bar{M}_0^{21} \mathbf{C}_{,1}^T \mathbf{N}_{,2} \right) dA \\
&\quad - \int_{\Omega_0^e} \left(\mathbf{N}_{,1}^T \mathbf{P}^{11} \mathbf{N}_{,1} + \mathbf{N}_{,2}^T \mathbf{P}^{22} \mathbf{N}_{,2} + \mathbf{N}_{,1}^T \mathbf{P}^{12} \mathbf{N}_{,2} + \mathbf{N}_{,2}^T \mathbf{P}^{21} \mathbf{N}_{,1} \right) dA \\
&\quad - \int_{\Omega_0^e} \left[\mathbf{N}_{,1}^T \mathbf{Q}^1 + \mathbf{N}_{,2}^T \mathbf{Q}^2 + (\mathbf{Q}^1)^T \mathbf{N}_{,1} + (\mathbf{Q}^2)^T \mathbf{N}_{,2} \right] dA,
\end{aligned} \tag{97}$$

where we have defined $b_M := b_{\alpha\beta} M_0^{\alpha\beta}$, and $\mathbf{Q}^\alpha := \mathbf{Q}^{\alpha\beta\gamma} \mathbf{N}_{,\beta\gamma}$. The last term \mathbf{k}_M^e is associated with in-plane bending.

Remark B.1: We note the term $a^{12} (\mathbf{L}_1^n \mathbf{L}_2^{nT} + \mathbf{L}_2^n \mathbf{L}_1^{nT})$ in \mathbf{k}_M^e is given incorrectly by $2 a^{12} \mathbf{L}_1^n \mathbf{L}_2^{nT}$ in Duong et al. [Duong et al. \(2017\)](#) (cf. Appendix B.1, Eq. (135.1)).

Acknowledgements

The authors are grateful to the German Research Foundation (DFG) for supporting this research under grants IT67/18-1 and SA1822/11-1. They thank Vu Ngoc Khiem for his fruitful comments on the material modeling.

References

- Ambati, M., Kiendl, J., and De Lorenzis, L. (2018). Isogeometric Kirchhoff–Love shell formulation for elasto-plasticity. *Comput. Methods Appl. Mech. Engrg.*, **340**:320–339.
- Asmanoglo, T. and Menzel, A. (2017). A multi-field finite element approach for the modelling of fibre-reinforced composites with fibre-bending stiffness. *Comput. Methods Appl. Mech. Engrg.*, **317**:1037–1067.
- Balobanov, V., Kiendl, J., Khakalo, S., and Niiranen, J. (2019). Kirchhoff–Love shells within strain gradient elasticity: Weak and strong formulations and an H3-conforming isogeometric implementation. *Comput. Methods Appl. Mech. Engrg.*, **344**:837–857.
- Barbagallo, G., Madeo, A., Azehaf, I., Giorgio, I., Morestin, F., and Boisse, P. (2017). Bias extension test on an unbalanced woven composite reinforcement: Experiments and modeling via a second-gradient continuum approach. *J. Compos. Mater.*, **51**(2):153–170.
- Battista, A., Rosa, L., dell’Erba, R., and Greco, L. (2017). Numerical investigation of a particle system compared with first and second gradient continua: Deformation and fracture phenomena. *Math. Mech. Solids*, **22**(11):2120–2134.
- Boisse, P., Borr, M., Buet, K., and Cherouat, A. (1997). Finite element simulations of textile composite forming including the biaxial fabric behaviour. *Compos. B. Eng.*, **28**(4):453–464.
- Boisse, P., Hamila, N., Guzman-Maldonado, E., Madeo, A., Hivet, G., and Dell’Isola, F. (2017). The bias-extension test for the analysis of in-plane shear properties of textile composite reinforcements and preregs: a review. *Int. J. Mater. Form.*, **10**:473–492.
- Boisse, P., Hamila, N., Helenon, F., Hagege, B., and Cao, J. (2008). Different approaches for woven composite reinforcement forming simulation. *Int J Mater Form*, **1**(1):21–29.
- Borden, M. J., Scott, M. A., Evans, J. A., and Hughes, T. J. R. (2011). Isogeometric finite element data structures based on Bezier extraction of NURBS. *Int. J. Numer. Meth. Engng.*, **87**:15–47.
- Cao, J., Akkerman, R., Boisse, P., Chen, J., Cheng, H. S., de Graaf, E. F., Gorczyca, J. L., Harrison, P., Hivet, G., Launay, J., Lee, W., Liu, L., Lomov, S. V., Long, A., de Luycker, E., Morestin, F., Padvoiskis, J., Peng, X. Q., Sherwood, J., Stoilova, T., Tao, X. M., Verpoest, I., Willems, A., Wiggers, J., Yu, T. X., and Zhu, B. (2008). Characterization of mechanical behavior of woven fabrics: Experimental methods and benchmark results. *Compos. Part A Appl. Sci. Manuf.*, **39**(6):1037–1053.
- D’Agostino, M. V., Giorgio, I., Greco, L., Madeo, A., and Boisse, P. (2015). Continuum and discrete models for structures including (quasi-) inextensible elasticae with a view to the design and modeling of composite reinforcements. *Int. J. Solids Struct.*, **59**:1–17.
- Deng, X., Korobenko, A., Yan, J., and Bazilevs, Y. (2015). Isogeometric analysis of continuum damage in rotation-free composite shells. *Comput. Methods Appl. Mech. Engrg.*, **284**:349–372. Isogeometric Analysis Special Issue.
- Duong, T. X. (2017). *Efficient contact computations based on isogeometric discretization, mortar methods and refined boundary quadrature*. PhD thesis, RWTH Aachen.
- Duong, T. X., Khiêm, V. N., Itskov, M., and Sauer, R. A. (2021). A general theory for anisotropic Kirchhoff–Love shells with embedded fibers and in-plane bending. *arXiv preprint, arXiv:2101.03122*.

- Duong, T. X., Roohbakhshan, F., and Sauer, R. A. (2017). A new rotation-free isogeometric thin shell formulation and a corresponding continuity constraint for patch boundaries. *Comput. Methods Appl. Mech. Engrg.*, **316**:43–83.
- Ferretti, M., Madeo, A., Dell’Isola, F., and Boisse, P. (2014). Modeling the onset of shear boundary layers in fibrous composite reinforcements by second-gradient theory. *Z. für Angew. Math. Phys.*, **65**:587–612.
- Germain, P. (1973). The method of virtual power in continuum mechanics. Part 2: Microstructure. *SIAM J. Appl. Math.*, **25**(3):556–575.
- Hughes, T. J. R., Cottrell, J. A., and Bazilevs, Y. (2005). Isogeometric analysis: CAD, finite elements, NURBS, exact geometry and mesh refinement. *Comput. Methods Appl. Mech. Engrg.*, **194**:4135–4195.
- Khiêm, V. N., Krieger, H., Itskov, M., Gries, T., and Stapleton, S. E. (2018). An averaging based hyperelastic modeling and experimental analysis of non-crimp fabrics. *Int. J. Solids Struct.*, **154**:43–54.
- Kiendl, J., Ambati, M., De Lorenzis, L., Gomez, H., and Reali, A. (2016). Phase-field description of brittle fracture in plates and shells. *Comput. Methods Appl. Mech. Engrg.*, **312**:374–394.
- Kiendl, J., Bletzinger, K.-U., Linhard, J., and Wüchner, R. (2009). Isogeometric shell analysis with Kirchhoff–Love elements. *Comput. Methods Appl. Mech. Engrg.*, **198**:3902–3914.
- Koiter, W. T. (1963). Couple-stresses in the theory of elasticity. *Philos. Trans. Royal Soc.*, **67**:17–44.
- Madeo, A., Barbagallo, G., D’Agostino, M. V., and Boisse, P. (2016). Continuum and discrete models for unbalanced woven fabrics. *Int. J. Solids Struct.*, **94–95**:263–284.
- Mindlin, R. D. (1965). Second gradient of strain and surface-tension in linear elasticity. *Int. J. Solids Struct.*, **1**(4):417–438.
- Mindlin, R. D. and Tiersten, H. F. (1962). Effects of couple-stresses in linear elasticity. *Arch. Rational Mech. Anal.*, **11**:415–488.
- Nagy, A. P., Ijsselmuiden, S. T., and Abdalla, M. M. (2013). Isogeometric design of anisotropic shells: Optimal form and material distribution. *Comput. Methods Appl. Mech. Engrg.*, **264**:145–162.
- Nguyen-Thanh, N., Kiendl, J., Nguyen-Xuan, H., Wüchner, R., Bletzinger, K.-U., Bazilevs, Y., and Rabczuk, T. (2011). Rotation free isogeometric thin shell analysis using PHT–splines. *Comput. Methods Appl. Mech. Engrg.*, **200**(47-48):3410–3424.
- Paul, K., Zimmermann, C., Duong, T. X., and Sauer, R. A. (2020). Isogeometric continuity constraints for multi-patch shells governed by fourth-order deformation and phase field models. *Comput. Methods Appl. Mech. Engrg.*, **370**:113219.
- Sauer, R. A. and Duong, T. X. (2017). On the theoretical foundations of solid and liquid shells. *Math. Mech. Solids*, **22**:343–371.
- Sauer, R. A., Duong, T. X., and Corbett, C. J. (2014). A computational formulation for constrained solid and liquid membranes considering isogeometric finite elements. *Comput. Methods Appl. Mech. Engrg.*, **271**:48–68.

- Sauer, R. A., Duong, T. X., Mandadapu, K. K., and Steigmann, D. J. (2017). A stabilized finite element formulation for liquid shells and its application to lipid bilayers. *J. Comput. Phys.*, **330**:436–466.
- Schulte, J., Dittmann, M., Eugster, S. R., Hesch, S., Reinicke, T., Dell’Isola, F., and Hesch, C. (2020). Isogeometric analysis of fiber reinforced composites using Kirchhoff-Love shell elements. *Comput. Methods Appl. Mech. Engrg.*, **362**:112845.
- Soldatos, K. P. (2010). Second-gradient plane deformations of ideal fibre-reinforced materials: implications of hyper-elasticity theory. *J. Eng. Math.*, **68**:99–127.
- Spencer, A. J. M. and Soldatos, K. P. (2007). Finite deformations of fibre-reinforced elastic solids with fibre bending stiffness. *Int. J. Nonlin. Mech.*, **42**(2):355–368.
- Steigmann, D. J. (1999). On the relationship between the Cosserat and Kirchhoff-Love theories of elastic shells. *Math. Mech. Solids*, **4**:275–288.
- Steigmann, D. J. (2012). Theory of elastic solids reinforced with fibers resistant to extension, flexure and twist. *Int. J. Nonlin. Mech.*, **47**(7):734–742.
- Steigmann, D. J. (2018). Equilibrium of elastic lattice shells. *J. Eng. Math.*, **109**:47–61.
- Steigmann, D. J. and Dell’Isola, F. (2015). Mechanical response of fabric sheets to three-dimensional bending, twisting, and stretching. *Acta. Mech. Sin.*, **31**:373–382.
- Tepole, A. B., Kabaria, H., Bletzinger, K.-U., and Kuhl, E. (2015). Isogeometric Kirchhoff-Love shell formulations for biological membranes. *Comput. Methods Appl. Mech. Engrg.*, **293**:328 – 347.
- Toupin, R. A. (1964). Theories of elasticity with couple-stress. *Arch. Rational Mech. Anal.*, **17**(2):85–112.
- Vu-Bac, N., Duong, T. X., Lahmer, T., Areias, P., Sauer, R. A., Park, H. S., and Rabczuk, T. (2019). A NURBS-based inverse analysis of thermal expansion induced morphing of thin shells. *Comput. Methods Appl. Mech. Engrg.*, **350**:480–510.
- Witt, C., Kaiser, T., and Menzel, A. (2021). A finite deformation isogeometric finite element approach to fibre-reinforced composites with fibre bending stiffness. *J. Eng. Math.*, **128**(1):15.
- Yu, W.-R., Harrison, P., and Long, A. (2005). Finite element forming simulation for non-crimp fabrics using a non-orthogonal constitutive equation. *Compos. - A: Appl. Sci. Manuf.*, **36**(8):1079–1093.
- Zimmermann, C., Toshniwal, D., Landis, C., Hughes, T. J. R., Mandadapu, K. K., and Sauer, R. A. (2019). An isogeometric finite element formulation for phase transitions on deforming surfaces. *Comput. Methods Appl. Mech. Engrg.*, **351**:441–477.
- Zou, Z., Hughes, T. J. R., Scott, M. A., Sauer, R. A., and Savitha, E. J. (2021). Galerkin formulations of isogeometric shell analysis: Alleviating locking with Greville quadratures and higher-order elements. *Comput. Methods Appl. Mech. Engrg.*, **380**:113757.